

# Independent Cosmological Constraints from high-*z* HII Galaxies <sup>\*</sup>

Ana Luisa González-Morán <sup>1,†</sup>, Ricardo Chávez <sup>1,2,3,4,‡</sup>, Roberto Terlevich <sup>1,5</sup>,  
Elena Terlevich <sup>1</sup>, Fabio Bresolin <sup>6</sup>, David Fernández-Arenas <sup>7,1</sup>, Manolis Plionis <sup>8,9</sup>,  
Spyros Basilakos <sup>8,10</sup>, Jorge Melnick <sup>11,12</sup> and Eduardo Telles <sup>12</sup>

<sup>1</sup> Instituto Nacional de Astrofísica, Óptica y Electrónica, Tonantzintla, C.P. 72840, Puebla, México

<sup>2</sup> Instituto de Radioastronomía y Astrofísica, UNAM, Campus Morelia, C.P. 58089, Morelia, México

<sup>3</sup> Cavendish Laboratory, University of Cambridge, 19 J. J. Thomson Ave, Cambridge, CB3 0HE, UK

<sup>4</sup> Kavli Institute for Cosmology, University of Cambridge, Madingley Road, Cambridge, CB3 0HA, UK

<sup>5</sup> Institute of Astronomy, University of Cambridge, Cambridge, CB3 0HA, UK

<sup>6</sup> Institute for Astronomy, University of Hawaii, 2680 Woodlawn Drive, 96822 Honolulu, HI USA

<sup>7</sup> Kavli Institute for Astronomy and Astrophysics, Peking University, Beijing 100871, China

<sup>8</sup> National Observatory of Athens, P.Pendeli, Athens, Greece

<sup>9</sup> Physics Dept., Aristotle Univ. of Thessaloniki, Thessaloniki 54124, Greece

<sup>10</sup> Academy of Athens Research Center for Astronomy & Applied Mathematics, Soranou Efessiou 4, 11-527 Athens, Greece

<sup>11</sup> European Southern Observatory, Santiago de Chile, Chile

<sup>12</sup> Observatorio Nacional, Rua José Cristino 77, 20921-400 Rio de Janeiro, Brasil

v118 — Compiled at 0:29 hrs on 7 June 2019

## ABSTRACT

We present new high spectral resolution observations of 15 high-*z* ( $1.3 \leq z \leq 2.5$ ) HII Galaxies (HIIG) obtained with MOSFIRE at the Keck Observatory. These data, combined with already published data for another 31 high-*z* and 107  $z \leq 0.15$  HIIG, are used to obtain new independent cosmological results using the distance estimator based on the established correlation between the Balmer emission line velocity dispersion and luminosity for HIIG. Our results are in excellent agreement with the latest cosmological concordance model ( $\Lambda$ CDM) published results. From our analysis, we find a value for the mass density parameter of  $\Omega_m = 0.290^{+0.056}_{-0.069}$  (stat). For a flat Universe we constrain the plane  $\{\Omega_m; w_0\} = \{0.280^{+0.130}_{-0.100}; -1.12^{+0.58}_{-0.32}\}$  (stat). The joint likelihood analysis of HIIG with other complementary cosmic probes (Cosmic Microwave Background and Baryon Acoustic Oscillations) provides tighter constraints for the parameter space of the Equation of State of Dark Energy that are also in excellent agreement with those of similar analyses using Type Ia Supernovae instead as the geometrical probe.

**Key words:** galaxies: starburst – observations – dark energy – cosmology: parameters

## 1 INTRODUCTION

The first clear evidence for an accelerated cosmic expansion was given by the analysis of Type Ia Supernovae (SNIa) data some 20 years ago (Riess et al. 1998; Perlmutter et al. 1999). Since then, analysis of the Cosmic Microwave Background (CMB) anisotropies (e.g. Jaffe et al. 2001; Pryke et al. 2002; Spergel et al. 2007; Planck Collaboration et al. 2014, 2016a) and of Baryon Acoustic Oscillations (BAOs) (e.g. Eisenstein et al. 2005; Blake et al. 2011) in combination with independent Hubble parameter measurements (e.g. Chávez et al. 2012; Freedman et al. 2012; Riess et al.

\* The new data presented in this paper were obtained using MOSFIRE at the W. M. Keck Observatory, which is operated as a scientific partnership among the California Institute of Technology, the University of California and the National Aeronautics and Space Administration. The Observatory was made possible by the generous financial support of the W. M. Keck Foundation.

† Contact e-mail: analuisagm@inaoep.mx

‡ Contact e-mail: r.chavez@irya.unam.mx

2016, 2018; Fernández Arenas et al. 2018) have provided ample evidence for the presence of what has been called the Dark Energy (DE) component of the Universe.

A main goal of present-day cosmology is to measure the DE Equation of State (EoS) and to explore its evolution (or lack of it) with look-back time as well as searching for hints of any other property of DE.

The cosmological parameters  $\Omega_m$ ,  $\Omega_\Lambda$  and  $w_0$  (plus  $w_a$  in the evolutive case) are obtained combining the low redshift results ( $z \lesssim 2$ ) for BAOs and SNIa (Riess et al. 1998; Perlmutter et al. 1999; Hicken et al. 2009; Amanullah et al. 2010; Riess et al. 2011; Suzuki et al. 2012; Betoule et al. 2014; Scolnic et al. 2018) with high redshift results ( $z \sim 1000$  Planck CMB fluctuations; e.g. Planck Collaboration et al. 2014, 2016a). This is because the individual solutions are degenerate and only combining them one can obtain competitive results. It is important to remark that there are no determinations of cosmological parameters at intermediate redshift ( $2 \lesssim z \lesssim 10$ ), where the maximum difference in cosmological models that include an evolving DE EoS occurs (cf. Plionis et al. 2011).

The  $L - \sigma$  relation between the emission line velocity dispersion ( $\sigma$ ) and the Balmer line luminosity ( $L[\text{H}\alpha]$ , usually  $\text{H}\beta$ ) of HII Galaxies (HIIG) has already been proven as a cosmological tracer (e.g. Melnick et al. 2000; Siegel et al. 2005; Plionis et al. 2011; Chávez et al. 2012, 2014; Terlevich et al. 2015; Chávez et al. 2016, and references therein). It has also been shown that the  $L(\text{H}\beta) - \sigma$  relation has been used in the local Universe to significantly constrain the value of  $H_0$  (Chávez et al. 2012; Fernández Arenas et al. 2018).

HIIG are a very promising tracer for the parameters of the DE EoS precisely because they can be observed, using the current available infrared instrumentation, up to  $z \sim 4$  (cf. Terlevich et al. 2015; Chávez et al. 2016). Even when their scatter on the Hubble-Lemaitre diagram is about a factor of two larger than in the case of high- $z$  SNIa, this disadvantage is compensated by the fact that HIIG are observed to much larger redshifts than SNIa where, as mentioned above, the degeneracies for different DE models are largely reduced (cf. Plionis et al. 2011). Chávez et al. (2016) presented simulations that predict substantial improvement in the constraints when increasing the sample of high- $z$  HIIG to 500, a goal that can be achieved in reasonable observing times with existing large telescopes and state-of-the-art instrumentation.

In this work, we use a new set of high spectral resolution observations of high- $z$  HIIG obtained with MOSFIRE at the Keck telescope to constrain in an independent manner cosmological parameters on the important range of intermediate redshift  $1.0 \lesssim z \lesssim 3.0$ . We increased the observed sample with selected data from the literature and apply both a standard  $\chi^2$  and a Markov Chain Monte Carlo (MCMC) methods to find the probability distribution of the solutions for a set of cosmological parameters and combine the results with those obtained using different probes (SNIa, BAOs, CMB).

This paper is organized as follows, §2 describes the data sample, our new data, its reduction process and analysis, and the extra data obtained from the literature. In §3 we discuss the extinction law applied to the data.

In §4 we present and discuss the results while the conclusions are given in §5. Serendipitous objects found in the

2D spectra, in Appendix A and the reduced 2D and 1D Keck spectra are shown in Appendix B.

## 2 DATA SAMPLE

### 2.1 MOSFIRE

The new high spectral resolution near-IR spectra presented in this work were obtained using MOSFIRE (McLean et al. 2010, 2012), the multi-object spectrograph at the Cassegrain focus of the 10-m Keck I telescope in Mauna Kea, Hawaii, during the night of January 27th, 2016. Candidate objects were selected from the literature according to 3 conditions:

- i) redshift ranges  $1.2 < z < 1.7$  and  $1.9 < z < 2.6$  in order to observe either  $\text{H}\alpha$  or  $\text{H}\beta$  and  $[\text{O III}]\lambda 5007\text{\AA}$  emission lines in the H band;
- ii) high equivalent widths (EW) in their emission lines; and
- iii) candidate belong to a dense cosmological field in order to have at least 10 HIIG in the MOSFIRE field of view.

As in our group's previous related papers, the second condition was selected because stellar population synthesis models for star-forming galaxies in bursting episodes (Leitherer et al. 1999), predict that if the  $\text{EW}(\text{H}\beta) > 50\text{\AA}$  ( $\text{EW}(\text{H}\alpha) > 200\text{\AA}$ ) the sample is composed by systems in which a single starburst younger than 5 Myr dominates the total luminosity. At the same time, this condition minimizes the contamination by an older underlying stellar population. To account for uncertainties in the measurements of EWs reported in the literature, we relaxed somehow the conditions so that the published values for the candidates were  $\text{EW}(\text{H}\beta) > 25\text{\AA}$  or  $\text{EW}(\text{H}\alpha) > 150\text{\AA}$ .

Since the  $\text{H}\beta$  line in these objects is in general weaker than the  $[\text{O III}]\lambda 5007\text{\AA}$  one, our selection criteria include also the  $[\text{O III}]$  line. If we assume that the  $\text{EW}[\text{O III}]$  behaves in the same way in HIIG at high as at low redshifts, we can use the  $F[\text{O III}]/F(\text{H}\beta)$  distribution of a sample of HIIG at low redshift in order to calculate statistically the distribution of the  $\text{EW}[\text{O III}]$  at high redshift through the relation:

$$\text{EW}[\text{O III}] = \frac{F[\text{O III}]}{F(\text{H}\beta)} \times \text{EW}(\text{H}\beta), \quad (1)$$

Using the result from Chávez et al. (2014) for a sample of 95 HIIG at low redshift having both  $F[\text{O III}]$  and  $F(\text{H}\beta)$  data, we adopted the selection criterion  $\text{EW}[\text{O III}] \gtrsim 400\text{\AA}$  for our new high redshift sample.

Following these criteria, we selected from Erb et al. (2006a,b); Tu et al. (2009); Mancini et al. (2011); Cooray et al. (2011); van der Wel et al. (2011); Bruce et al. (2012); Brammer et al. (2012); Lundgren et al. (2012); Maseda et al. (2013, 2014) a sample of 35 candidates for our MOSFIRE run in the GOODS North (GOODS-N; Giavalisco et al. 2004), the Cosmic Evolution Survey (COSMOS; Scoville et al. 2007; Koekemoer et al. 2007) and the Ultra Deep Survey (UDS; Lawrence et al. 2007; Cirasuolo et al. 2007) fields. The observed sample is detailed in Table 1. The target name is given in the first column; the coordinates in the second and third column; the cosmological field that each object belongs to in column 4; the seeing in arcseconds during the observations of each field in column 5; the total exposure

**Table 1.** Observed sample.

Name	R.A. (J2000)	DEC. (J2000)	Field	PSF (arcsec)	Exp. time (seconds)	Ref.
HDF-BX1376	12 36 52.962	62 15 45.70	GOODS-N	0.79''	10,560	1,2
HDF-BX1368	12 36 48.249	62 15 56.43				1,2
HDF-BX1409	12 36 47.408	62 17 28.77				1,2
HDF-BX305	12 36 37.105	62 16 28.71				1,2
HDF-BX1311	12 36 30.522	62 16 26.15				1,2
HDF-BX1388	12 36 44.832	62 17 15.88				1,2
3D-HST10245	12 36 23.280	62 15 28.00				3
UDS9	02 17 31.822	-05 14 40.70	UDS	0.58''	7,200	4
UDS23	02 17 32.882	-05 10 38.06				4
UDS25	02 17 36.514	-05 10 31.31				4
UDS40	02 17 45.146	-05 09 36.34				4
UDS-14655	02 17 33.926	-05 11 43.08				5,6
UDS-11484	02 17 43.536	-05 12 43.60				5,6
UDS-12435	02 17 38.607	-05 14 05.36				6
UDS-10138	02 17 41.606	-05 14 32.13				6
UDS-4501	02 17 33.783	-05 15 02.87				5,6
UDS-109082	02 17 37.392	-05 13 07.88				7
UDS-112374	02 17 32.544	-05 11 56.32				7
UDS-113972	02 17 40.353	-05 11 16.80				7
UDS-116891	02 17 39.784	-05 10 18.75				7
UDS-118417	02 17 35.301	-05 09 43.54				7
Lensed target2	02 17 37.237	-05 13 29.78				8,9,10
COSMOS-16207	10 00 43.937	02 22 22.53	COSMOS	0.64''	10,080	5,6
COSMOS-13848	10 00 42.478	02 20 43.42				5,6
COSMOS-16566	10 00 40.960	02 20 53.86				6
COSMOS-18358	10 00 40.120	02 22 00.63				6
COSMOS-12807	10 00 38.295	02 19 59.92				5,6
COSMOS-15144	10 00 37.629	02 21 38.79				5,6
COSMOS-17118	10 00 36.277	02 21 14.89				6
COSMOS-19049	10 00 33.333	02 22 24.16				6
COSMOS13073	10 00 29.954	02 22 56.23				11
COSMOS32915	10 00 35.087	02 22 27.30				11
COSMOS133784	10 00 31.031	02 22 10.44				12
COSMOS134172	10 00 26.463	02 22 26.84				12
zCOSMOS-411737	10 00 32.356	02 21 21.00				13

References: (1): Erb et al. (2006a); (2): Erb et al. (2006b), (3): Lundgren et al. (2012); (4): van der Wel et al. (2011); (5): Maseda et al. (2013); (6): Maseda et al. (2014); (7): Bruce et al. (2012); (8): Brammer et al. (2012); (9): Tu et al. (2009); (10): Cooray et al. (2011); (11) Belli et al. (2014); (12): Krogager et al. (2014); (13): Mancini et al. (2011).

time per field in seconds in column 6 and in column 7 the literature reference for the sample objects.

### 2.1.1 Observations and Data Reduction

MOSFIRE has a cryogenic configurable slit unit (CSU), consisting of 46 pairs of bars each one of length  $7.1''$ . The bars can be configured in the direction perpendicular to the slits anywhere within an effective field of view of  $3' \times 6'$ .

We designed our masks using MAGMA<sup>1</sup>. The wavelength coverage of the spectra depends on the position of the slit in the CSU, thus it differs slightly from target to target. Therefore, the standard star must be observed in two

wavelength settings (POS A and POS C) to guarantee the full coverage of the wavelength range of the science targets.

The high resolution spectra ( $R = 5,340$  in the H band) were obtained using a  $0.48''$  slit width. Total exposure times per cosmological field ranged between 2 and 3 hrs. For each run we measured the point spread function (PSF) from Gaussian fits to the spatial profile of stars observed simultaneously in the three fields. The resulting FWHM of the PSF ranges between  $0.5''$  and  $0.8''$  measured in the H band (see Table 1).

To identify each target we used the images from the Cosmic Assembly Near-IR Deep Extragalactic Legacy Survey (CANDELS), Multi-Cycle Treasury Program with the NASA/ESA HST (Grogin et al. 2011; Koekemoer et al. 2011) in the filter f160w corresponding to the H band. The slit orientations were 96, 10 and 114 degrees for the COSMOS, UDS and GOODS-N fields, respectively. Since all slit widths were  $0.48''$ , the compactness of the sources can be appreciated in Figure 1. For  $\Lambda$ CDM cosmology and  $H_0 =$

<sup>1</sup> MAGMA (MOSFIRE Automatic GUI-based Mask Application) is a tool that is used to design new slitmasks for use with MOSFIRE and is available from the website <http://www2.keck.hawaii.edu/inst/mosfire/magma.html>.

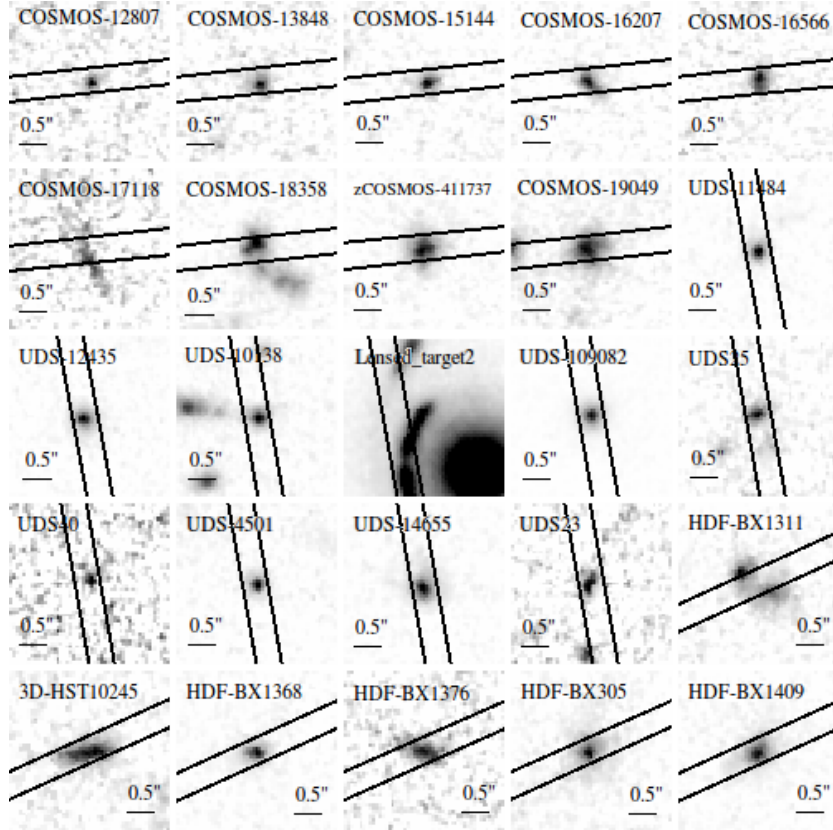


**Figure 1.** Target images in the f160w filter (H band) from CANDELS HST Program. Superposed are the slits with the orientation and width set for the MOSFIRE observations. The slit width of  $0.48''$  represents (for a  $\Lambda$ CDM cosmology and  $H_0=71$  km/s Mpc $^{-1}$ ) a physical scale of  $\sim 4$  kpc.

71 km/s Mpc $^{-1}$ , the scale at  $z = 1.55$  is 8.3 kpc/arcsec and at  $z = 2.3$  is 8.1 kpc/arcsec. Thus the  $0.48''$  slit represents a metric scale of  $\sim 4$  kpc.

The data reduction was carried out using the MOSFIRE Data Reduction Pipeline (DRP) developed by the MOSFIRE team<sup>2</sup>. The MOSFIRE DRP produces flat-field corrected, background subtracted, wavelength calibrated, and rectified 2D spectra for each slit on a given mask. The 2D wavelength solutions in the H band were obtained from the night sky OH emission lines for each slit.

The final product of the MOSFIRE DRP is wavelength calibrated 2D spectra. The one-dimensional (1D) spectra and the flux calibration were obtained using IRAF<sup>3</sup>. For the flux calibration, we need to select either POS A or POS C of the reference star spectra. So, depending on the redshift and slit position of each target on the field of view, the wavelength coverage of the spectra differs.

The wavelength range of POS A is from 15,200Å to 17,730Å for the UDS field and from 15,160Å to 17,920Å for the GOODS-N field while POS C goes from 15,000Å to 17,350Å for all the fields.

<sup>2</sup> <http://www2.keck.hawaii.edu/inst/mosfire/drp.html>.

<sup>3</sup> IRAF (Image Reduction and Analysis Facility) is a software for the reduction and analysis of astronomical data. It is written and supported by the National Optical Astronomy Observatories (NOAO).

### 2.1.2 Redshifts

Emission lines were detected in 25 of the 35 candidates. The sample of 25 HIIG contains 11 objects at  $z \sim 2.3$  and 14 at  $z \sim 1.5$ .

To determine the redshift and width of the emission lines we fitted  $H\alpha$  for the objects at  $z \sim 1.5$  and [O III] $\lambda\lambda 4959, 5007$  Å and  $H\beta$  for the objects at  $z \sim 2.3$ . An example of the Gaussian fitting to the  $H\alpha$  line for the target COSMOS-16566 is shown in Figure 2.

For the objects at  $z \sim 2.3$  the redshifts were measured using at least 2 emission lines. For those which have only one emission line (objects at  $z \sim 1.5$ ) we compared our values with those from the literature that have been measured using other lines. Three objects in the UDS field (UDS23, UDS25 and UDS40) were selected from their photometric redshift indicating [O III] emission in the redshift range  $1.6 < z < 1.8$  (van der Wel et al. 2011). Our MOSFIRE/Keck data shows a strong line detection that we identified as  $H\alpha$  at a redshift  $z=1.6113$  for UDS40,  $z=1.6658$  for UDS25 and  $z=1.6001$  for UDS23 thus confirming the photometric estimate.

As a result, 24 of the 25 measured redshifts coincide with those reported in the literature with small variations of  $\pm 0.001$ . For the remaining object, UDS-109082, we found variations of +0.23 and -0.05 with respect to the published redshift; combining this difference in redshift with the fact that in our spectrum only one emission line is present, we assume that the observed line is  $H\alpha$  at redshift 1.6814.

The redshifts measured for each line are shown in columns 2, 3, 4 and 5 of Table 2 and the 2D and 1D spectra and the Gaussian fits to the emission lines are shown in Appendix B.

### 2.1.3 Velocity Dispersions

We have measured the velocity dispersion ( $\sigma$ ) of the ionized gas from Gaussian fits to the emission lines. The  $\sigma$  of the observed profile being,

$$\sigma_{obs} = \frac{FWHM}{2\sqrt{2\ln 2}}, \quad (2)$$

where FWHM is the full width at half-maximum of the emission line. The uncertainties were estimated using a Monte-carlo analysis where a set of random realizations of each spectrum was generated using the r.m.s. intensity of the continuum adjacent to the emission line (see Figure 2). The FWHM  $1\sigma$  uncertainty was estimated from the standard deviation of the distribution of FWHM measurements. The fit to the observed lines and the distribution of FWHM obtained from the Monte-carlo simulations are also shown in figures B1 and B2.

The sigma of the observed profile for each line can be broken down into four components:

$$\sigma_{obs}^2 = \sigma^2 + \sigma_{th}^2 + \sigma_i^2 + \sigma_{fs}^2, \quad (3)$$

where  $\sigma_{th}$ ,  $\sigma_i$  and  $\sigma_{fs}$  are the thermal, instrumental and fine structure broadening components, respectively, and  $\sigma$  is the intrinsic velocity dispersion. The thermal broadening can be calculated from the expression:

$$\sigma_{th} = \sqrt{\frac{kT_e}{m}}, \quad (4)$$

where  $k$  is the Boltzmann constant,  $m$  is the mass of the ion in question and  $T_e$  is the electron temperature in degrees Kelvin, for which a reasonable value is  $T_e = 10,000$  K.

For the fine structure width, which is important for hydrogen recombination lines but not for metal lines such as [O III], we adopted a value of  $\sigma_{fs}^2(\text{H}\alpha) = 10.233 \text{ km}^2 \text{ s}^{-2}$  or  $\sigma_{fs}^2(\text{H}\beta) = 5.767 \text{ km}^2 \text{ s}^{-2}$  (García-Díaz et al. 2008). Finally, the instrumental broadening is measured from the sky lines width giving a value of  $\sigma_i = 22.68 \text{ km s}^{-1}$ .

Summarizing, we determine the one-dimensional (1D) velocity dispersion by fitting a Gaussian profile to each emission line and from those values subtracting in quadrature the thermal, instrumental and fine structure broadening using Equation 3. The resulting values of the velocity dispersion for each emission line are given in  $\text{km s}^{-1}$  in columns 3, 4, 5 and 6 of Table 3.

### 2.1.4 Fluxes

The star observed (HD225023) is a photometric (not spectrophotometric) standard. In order to calibrate in flux we used its observed spectrum combined with a black-body curve corresponding to its spectral type (A0 star with a magnitude  $H=6.985$  in the CIT/CTIO system by Elias et al. (1982)). We applied the extinction curve for Mauna Kea,

Hawaii, in the bands J, H, K', Ks and K, respectively for 2.2 mm of precipitable water vapour.

To verify our calibration, we applied it to the observed star spectrum. We obtained for POS A an H band flux at effective wavelength  $1.65 \mu\text{m}$  of  $F_{1.65\mu\text{m}} = 1.846 \times 10^{-13} \text{ erg s}^{-1} \text{ cm}^{-2} \text{ \AA}^{-1}$  for the UDS field,  $F_{1.65\mu\text{m}} = 1.829 \times 10^{-13} \text{ erg s}^{-1} \text{ cm}^{-2} \text{ \AA}^{-1}$  for the COSMOS field,  $F_{1.65\mu\text{m}} = 1.824 \times 10^{-13} \text{ erg s}^{-1} \text{ cm}^{-2} \text{ \AA}^{-1}$  for the GOODS-N field. For the POS C corresponding to the COSMOS, UDS and GOODS-N fields we obtained  $F_{1.65\mu\text{m}} = 1.869 \times 10^{-13} \text{ erg s}^{-1} \text{ cm}^{-2} \text{ \AA}^{-1}$ .

We converted the  $m_H=6.985$  to flux using the equation:

$$F_\nu = F_0 10^{-6.985/2.5}, \quad (5)$$

where  $F_0 = 980$  Jy corresponds to the CIT/CTIO system. Transforming  $F_\nu$  to  $F_\lambda$  using the equation:

$$F_\lambda = F_\nu \frac{c}{\lambda^2}, \quad (6)$$

with an effective wavelength of  $1.65 \mu\text{m}$ , we obtained  $F_{1.65\mu\text{m}} = 1.730 \times 10^{-13} \text{ erg s}^{-1} \text{ cm}^{-2} \text{ \AA}^{-1}$ . We conclude that the science targets calibrated with the standard star observed in the POS A for the UDS, COSMOS and GOODS-N fields have a flux uncertainty due to the calibration method of 7%, 6% and 5%, respectively. The science targets calibrated with the standard star observed in the POS C for the 3 cosmological fields have a flux uncertainty due to the calibration method of 8% with respect to their total flux.

The emission line fluxes were measured using the IRAF task *splot* and their uncertainties were estimated from the expression:

$$\epsilon_{Flux} = \sqrt{\epsilon_F^2 + \epsilon_{calF}^2}, \quad (7)$$

where  $\epsilon_{calF}$  is the uncertainty due to the flux calibration process and  $\epsilon_F$  was calculated from the expression (Tresse et al. 1999):

$$\epsilon_F = \epsilon_c D \sqrt{2N_{pix} + EW/D}, \quad (8)$$

where  $\epsilon_c$  is the mean standard deviation per pixel of the continuum at each side of the line,  $D$  is the spectral dispersion in  $\text{\AA}/\text{pixel}$ ,  $N_{pix}$  is the number of pixels covered by the line and  $EW$  is the rest equivalent width in  $\text{\AA}$  estimated also by using the IRAF task *splot*. The  $EW$  uncertainties were estimated as (Tresse et al. 1999):

$$\epsilon_{EW} = \frac{EW}{F} \epsilon_c D \sqrt{EW/D + 2N_{pix} + (EW/D)^2/N_{pix}}, \quad (9)$$

where  $F$  is the flux in  $\text{ergs s}^{-1} \text{ cm}^{-2}$ .

The  $EW$ s are shown in columns 6, 7, 8 and 9 of Table 2 and the measured fluxes are listed in columns 7, 8, 9 and 10 of Table 3. Our measurements are in good agreement with three of the four objects with published values (see Table 4). For reasons discussed in Section 2.2 and in Appendix A, the discordant object has been excluded from the analysis, as indicated in Table 3.

## 2.2 Excluded objects

Following Chávez et al. (2014) and Terlevich et al. (2015) we have selected only those HIIG which have high equiva-

**Table 2.** Measured redshifts and EWs

Name	z[O III] λ5007Å	z[O III] λ4959Å	z(Hβ)	z(Hα)	EW[O III] λ5007Å	EW[O III] λ4959Å	EW(Hβ)	EW(Hα)
HDF-BX1376	2.4293	2.4291	2.4297	...	218±49	88±13	77±24	...
HDF-BX1368	2.4412	2.4412	2.4403	...	342±45	166±37	67±14	...
HDF-BX1409	2.2457	2.2460	2.2463	...	236±54	37±9	45±9	...
HDF-BX305	2.4833	2.4832	2.4843	...	135±12	76±17	45±6	...
HDF-BX1311	2.4840	2.4840	2.4845	...	285±43	154±50	63±14	...
3D-HST10245	...	...	...	1.3592	...	...	...	172±48
UDS40	...	...	...	1.6113	...	...	...	...
UDS25	...	...	...	1.6658	...	...	...	243±102
UDS23	...	...	...	1.6001	...	...	...	194±140
UDS-14655	2.2983	2.2988	2.2989	...	443±115	124±49	61±9	...
UDS-11484	2.1855	2.1856	2.1858	...	672±118	109±28	67±32	...
UDS-109082	...	...	...	1.6814	...	...	...	249±141
Lensed target2	2.2868	2.2867	2.2874	...	72±13	30±5	27±12	...
UDS-12435	...	...	...	1.6114	...	...	...	224±67
UDS-10138	2.1510	2.1511	2.1511	...	411±161	97±26	63±18	...
UDS-4501	2.2973	2.2973	...	...	576±243	106±20	...	...
COSMOS-16207	...	...	...	1.6482	...	...	...	256±52
COSMOS-13848	...	...	...	1.4433	...	...	...	213±122
COSMOS-16566	...	...	...	1.4366	...	...	...	248±89
COSMOS-18358	...	...	...	1.6491	...	...	...	166±24
COSMOS-12807	...	...	...	1.5820	...	...	...	230±90
COSMOS-15144	...	...	...	1.4120	...	...	...	248±72
COSMOS-17118	...	...	...	1.6554	...	...	...	244±106
COSMOS-19049	...	...	...	1.3688	...	...	...	169±32
zCOSMOS-411737	2.4451	2.4453	2.4454	...	334±48	69±10	67±7	...

Redshifts measured using Gaussian fits with the PYTHON routine mpfit (<https://www.scipy.org/citing.html>)  
Equivalent widths measured using the IRAF task splot.

**Table 3.** Redshift, velocity dispersions and fluxes of the relevant lines.

Name	z <sup>a</sup>	σ[O III] <sup>b</sup> λ5007Å	σ[O III] <sup>b</sup> λ4959Å	σ(Hβ) <sup>b</sup>	σ(Hα) <sup>b</sup>	F[O III] <sup>c</sup> <sub>obs</sub> λ5007Å	F[O III] <sup>c</sup> <sub>obs</sub> λ4959Å	F(Hβ) <sup>c</sup> <sub>obs</sub>	F(Hα) <sup>c</sup> <sub>obs</sub>
†HDF-BX1376	2.4294	58.1±3.5	51.2±4.9	43.6±11.9	...	6.48±0.60	2.03±0.19	1.33±0.23	...
HDF-BX1368	2.4409	122.3±4.1	124.1±8.0	42.6±4.1	...	13.83±0.88	5.44±0.55	2.10±0.24	...
HDF-BX1409	2.2460	102.7±7.7	62.7±7.0	145.6±19.3	...	5.46±0.64	0.96±0.17	1.30±0.21	...
HDF-BX305	2.4836	76.9±3.1	109.0±23.7	125.0±16.9	...	6.21±0.45	2.39±0.36	1.95±0.22	...
HDF-BX1311	2.4842	97.4±4.0	85.3±16.4	147.0±24.0	...	9.04±0.95	2.99±0.46	2.08±0.32	...
†3D-HST10245	1.3592	...	...	...	73.9±6.4	...	...	...	4.03±0.50
†UDS40	1.6113	...	...	...	58.8±10.2	...	...	...	1.50±0.23
†UDS25	1.6658	...	...	...	56.7±3.9	...	...	...	4.77±0.74
†UDS23	1.6001	...	...	...	44.7±5.3	...	...	...	1.14±0.26
UDS-14655	2.2986	62.4±2.2	51.6±3.5	33.7±6.6	...	11.32±1.16	3.07±0.48	1.50±0.17	...
†UDS-11484	2.1856	62.5±1.5	75.4±8.4	67.7±17.2	...	18.83±1.54	6.06±0.81	2.08±0.54	...
†UDS-109082	1.6814	...	...	...	58.2±10.7	...	...	...	2.58±0.52
Lensed target2	2.2869	58.7±5.3	41.6±18.1	52.3±10.6	...	3.47±0.42	1.41±0.19	0.61±0.20	...
†UDS-12435	1.6114	...	...	...	67.5±5.5	...	...	...	4.87±0.63
UDS-10138	2.1511	68.0±3.8	71.8±8.1	84.5±12.6	...	11.41±1.56	4.49±0.69	2.25±0.39	...
UDS-4501	2.2973	77.4±3.2	73.3±7.5	...	...	9.89±1.18	4.44±0.53	1.15±0.33	...
†COSMOS-16207	1.6482	...	...	...	42.4±1.5	...	...	...	6.87±0.61
†COSMOS-13848	1.4433	...	...	...	28.0±5.4	...	...	...	1.28±0.21
†COSMOS-16566	1.4366	...	...	...	41.4±2.3	...	...	...	3.65±0.41
†COSMOS-18358	1.6491	...	...	...	66.2±4.0	...	...	...	10.99±0.97
†COSMOS-12807	1.5820	...	...	...	53.3±4.8	...	...	...	1.88±0.23
†COSMOS-15144	1.4120	...	...	...	45.2±2.2	...	...	...	6.94±0.71
†COSMOS-17118	1.6554	...	...	...	31.8±3.3	...	...	...	3.56±0.44
COSMOS-19049	1.3688	...	...	...	117.9±10.1	...	...	...	6.11±0.63
zCOSMOS-411737	2.4453	81.2±2.6	72.9±6.4	75.6±5.4	...	10.53±0.76	2.92±0.28	2.24±0.20	...

Flux in  $10^{-17}$  erg s<sup>-1</sup> cm<sup>-2</sup> and velocity dispersion in km/s.

Typical uncertainties in redshift are  $\sim 10^{-4}$ .

<sup>a</sup> Mean redshift.

<sup>b</sup> Gaussian fits done using the PYTHON routine mpfit.

<sup>c</sup> Measurements done using the IRAF task splot.

† HIIG selected for the cosmological analysis.

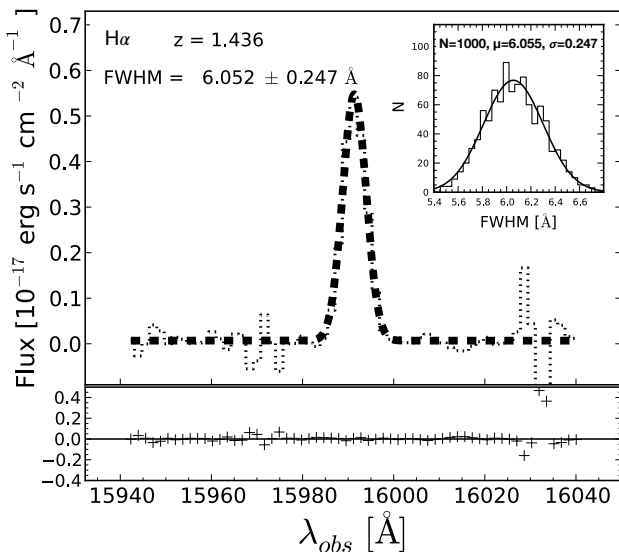


**Figure 2.**  $H\alpha$  line for COSMOS-16566. The dashed grey line is the spectrum, the dashed dark line is the Gaussian fit to the emission line and the box underneath shows the residuals. The inset at the upper right corner is the Monte Carlo analysis performed to the line where the standard deviation of the resulting distribution is taken as the uncertainty of the measured FWHM of the Gaussian fit.

**Table 4.** Observed [O III] fluxes; This work vs. literature.

Name	Flux[O III] $\lambda$ 5007 <sup>a</sup> this work	Flux[O III] $\lambda$ 5007 <sup>b</sup> literature
UDS-14655	11.3 $\pm$ 1.2	21.9 $\pm$ 3.1
UDS-11484	18.8 $\pm$ 1.5	21.5 $\pm$ 2.8
UDS-10138	11.4 $\pm$ 1.6	10.9 $\pm$ 0.6
UDS-4501	9.9 $\pm$ 1.2	13.7 $\pm$ 2.8

Flux in units of  $10^{-17}$  erg  $s^{-1}$   $cm^{-2}$ .

<sup>a</sup> Measured using the IRAF task `splot`.

<sup>b</sup> Fluxes taken from Maseda et al. (2013, 2014).

lent width in their emission lines and a logarithmic velocity dispersion,  $\log \sigma + \text{error} \leq 1.84$ .

We have excluded two additional objects, HDF-BX1368 and UDS-14655 on the grounds of having  $H\beta$  contaminated by a sky emission line. In principle it would be possible to use  $\sigma[\text{O III}]$  instead of  $\sigma(H\beta)$  as in Terlevich et al. (2015). However, due to the sky contamination it is not possible to accurately determine the  $H\beta$  fluxes to combine with the  $\sigma[\text{O III}]$  (cf Melnick et al. 2017). A third excluded object, Lensed target2, belongs to the UDS-01 Lensing system (SL2SJ02176-0513; Tu et al. 2009; Cooray et al. 2011; Brammer et al. 2012), which is an uncommon quite complex lens system showing two multiply-imaged systems at different redshifts lensed by a foreground massive galaxy at  $z_{lens} = 0.656$ : a bright cusp arc at  $z_{arc} = 1.847$  and an additional double-image system at  $z_{dbl} = 2.29$  estimated by Brammer et al. (2012). It is interesting that we detect the  $\text{HeI}\lambda 5876$  Å emission line confirming the reported redshift of the bright cusp arc of  $z = 1.847$  (see Appendix A) and  $H\beta$  and  $[\text{O III}]\lambda\lambda 4959, 5007$  Å which confirm the reported redshift of the double-image system of  $z = 2.29$ . We labelled

this galaxy as Lensed target 2 since it is the second gravitationally lensed object in the lensing system (see Table 3 and Figure 1). As a confirmed complex gravitational lens we decided to remove it from the analysis.

All this reduces the MOSFIRE sample to the 15 objects indicated with a dagger symbol in Table 3.

### 2.3 Literature sample

In order to increase the sample we have added published HIIG data following the same selection criteria.

a) At low  $z$  ( $0.01 \leq z \leq 0.15$ ) 107 HIIG extensively analysed in Chávez et al. (2014).

b) At intermediate and high- $z$  ( $0.6 \leq z \leq 2.5$ ) we included 25 HIIG from Erb et al. (2006a), Masters et al. (2014) and Maseda et al. (2014) plus our 6 HIIG observed with VLT-XShooter published in Terlevich et al. (2015).

The total number of HIIG used for the remainder of this paper is thereby 153.

## 3 EXTINCTION CORRECTION

The extinction correction was performed using two different laws: the one by Calzetti et al. (2000), which has been widely used for massive starburst galaxies; and that of Gordon et al. (2003), that corresponds to the Large Magellanic Cloud (LMC) supershell near the prototypical Giant HII Region (GHIIR) 30 Doradus in the LMC.

The extinction corrected fluxes were determined, as is the usual practice, from the expression:

$$F(\lambda) = F_{obs}(\lambda) 10^{0.4Avk(\lambda)/Rv}, \quad (10)$$

where  $k(\lambda) = A(\lambda)/E(B - V)$  is given by the extinction law used. We adopt  $k(H\beta) = 3.33$  and  $k(H\alpha) = 2.22$  or  $k(H\beta) = 4.60$  and  $k(H\alpha) = 3.32$  for Gordon et al. (2003) and Calzetti et al. (2000), respectively.

Given the redshifts of the objects observed with MOSFIRE, and as we only have H band data, we cannot measure the Balmer decrement directly. Instead the extinction ( $A_v$ ) was derived from the published  $E(B - V)$  whenever available, using the value of  $R_v = 2.77$  given by Gordon et al. (2003) or  $R_v = 4.05$  given by Calzetti et al. (2000) extinction curves. For those objects where the reddening was not available the mean  $A_v/R_v = 0.2208$  or  $0.1454$  from our local sample was adopted for Gordon et al. (2003) or Calzetti et al. (2000), respectively.

In Figure 3 we present the dust attenuation curves for different samples of star-forming galaxies. It is clear from the figure that the dust attenuation curve derived from analogs of high redshift star forming galaxies given by Salim et al. (2018) (long-dashed blue line) and from star forming galaxies at  $z \sim 2$  given by Reddy et al. (2015) (dot-dashed green line) agrees quite well with the Large and Small Magellanic Clouds slopes given by Gordon et al. (2003) (dotted orange and dotted short-dashed red lines). Therefore, for our sample of HIIG at high redshift we prefer the results obtained using the Gordon et al. (2003) extinction curve for the supershell in the Large Magellanic Cloud. However, to facilitate the comparison with our previous work we also present the results using Calzetti et al. (2000) law.

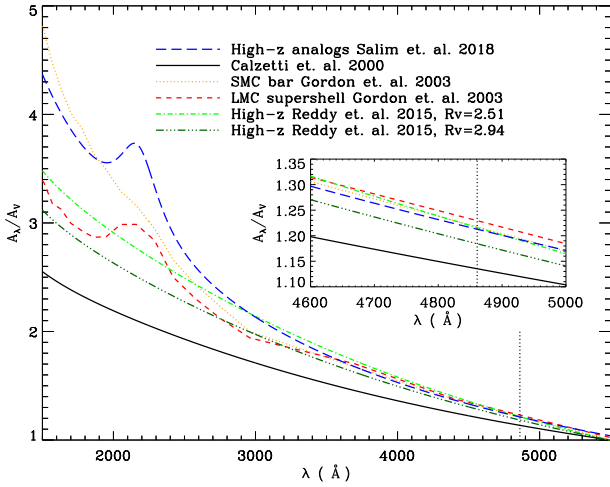


**Figure 3.** Dust attenuation curves for different samples of star-forming galaxies. The inset show a zoom between 4600Å and 5000Å. The vertical dotted line indicates the position of  $H\beta$ .

## 4 RESULTS AND DISCUSSION

### 4.1 Constraining cosmological parameters with HIIG

To calculate the parameters of the  $L - \sigma$  relation in a unified way including HIIG and GHIIR, we define the following likelihood function:

$$\mathcal{L}_{HII} \propto \exp\left(-\frac{1}{2}\chi_{HII}^2\right), \quad (11)$$

where:

$$\chi_{HII}^2 = \sum_n \frac{(\mu_o(\log f, \log \sigma | \alpha, \beta) - \mu_\theta(z | \theta))^2}{\epsilon^2}. \quad (12)$$

where  $\mu_o$  is the distance modulus calculated from a set of observables as:

$$\mu_o = 2.5(\alpha + \beta \log \sigma - \log f - 40.08), \quad (13)$$

where  $\alpha$  and  $\beta$  are the  $L - \sigma$  relation's intercept and slope, respectively,  $\log \sigma$  is the logarithm of the measured velocity dispersion and  $\log f$  is the logarithm of the measured flux.

For HIIG the theoretical distance modulus,  $\mu_\theta$ , is given as:

$$\mu_\theta = 5 \log d_L(z, \theta) + 25, \quad (14)$$

where  $z$  is the redshift,  $d_L$  is the luminosity distance in Mpc and  $\theta$  is a given set of cosmological parameters.

For GHIIR, the value of  $\mu_\theta$  is inferred from primary indicators. The GHIIR sample is described in detail in Fernández Arenas et al. (2018).

Finally  $\epsilon^2$ , the weights in the likelihood function, can be given as:

$$\epsilon^2 = \epsilon_{\mu_o, stat}^2 + \epsilon_{\mu_\theta, stat}^2 + \epsilon_{sys}^2, \quad (15)$$

where  $\epsilon_{stat}$  are the statistical uncertainties given as:

$$\epsilon_{\mu_o, stat}^2 = 6.25(\epsilon_{\log f}^2 + \beta^2 \epsilon_{\log \sigma}^2 + \epsilon_\beta^2 \log \sigma^2 + \epsilon_\alpha^2), \quad (16)$$

where  $\epsilon_{\log f}$ ,  $\epsilon_{\log \sigma}$  and  $\epsilon_\alpha$  are the uncertainties associated with the logarithm of the flux, the logarithm of the velocity dispersion and the intercept of the  $L - \sigma$  relation respectively

and  $\epsilon_{\mu_\theta, stat}$  in equation 15 is the uncertainty associated with the distance modulus as propagated from the redshift uncertainty in the case of HIIG and for the case of GHIIR as given by the cepheid measurements uncertainty. Finally,  $\epsilon_{sys}$  are the systematic uncertainties as described in Chávez et al. (2016) mentioned for completeness but not included in the present analysis (see also section 4.1.1)

Using the likelihood function given in Equation 11 in the MultiNest Bayesian inference algorithm (cf. Feroz & Hobson 2008; Feroz et al. 2009, 2013), we estimate the parameters of the  $L - \sigma$  relation for the sample of 107 local ( $0.01 \leq z \leq 0.15$ ) HIIG discussed in §2.3 and 36 GHIIR at  $z \leq 0.01$  described in Fernández Arenas et al. (2018) for which distances have been estimated from primary indicators, both samples corrected for extinction using the Gordon et al. (2003) extinction curve (see §3). The resulting parameters are:

$$\alpha = 33.268 \pm 0.083 \quad (17)$$

$$\beta = 5.022 \pm 0.058. \quad (18)$$

The  $L - \sigma$  relation shown in Figure 4, includes the new data for high- $z$  objects presented in §2.1 and those analysed previously in Terlevich et al. (2015) and Chávez et al. (2016).

In order to compare with Chávez et al. (2016) results, we also used their  $\alpha$  and  $\beta$  parameters derived after correcting the data for extinction using the Calzetti et al. (2000) curve:

$$\alpha = 33.11 \pm 0.145 \quad (19)$$

$$\beta = 5.05 \pm 0.097. \quad (20)$$

The luminosity distance  $d_L$  of the sources tracing the Hubble expansion is employed to calculate the theoretical distance moduli (see Equation 14). We define, for convenience, an extra parameter independent of the Hubble constant as:

$$D_L(z, \theta) = (1+z) \int_0^z \frac{dz'}{E(z', \theta)}. \quad (21)$$

i.e.,  $d_L = cD_L/H_0$ .  $E(z, \theta)$  for a flat Universe is given by:

$$E^2(z, \theta) = \Omega_r(1+z)^4 + \Omega_m(1+z)^3 + \Omega_w(1+z)^{3y} \exp\left(\frac{-3w_a z}{1+z}\right) \quad (22)$$

with  $y = (1 + w_0 + w_a)$ . The parameters  $w_0$  and  $w_a$  refer to the DE EoS, the general form of which is:

$$p_w = w(z)\rho_w, \quad (23)$$

with  $p_w$  the pressure and  $\rho_w$  the density of the postulated DE fluid. Different DE models have been proposed and many are parametrized using a Taylor expansion around the present epoch:

$$w(a) = w_0 + w_a(1-a) \implies w(z) = w_0 + w_a \frac{z}{1+z}, \quad (24)$$

(CPL model; Chevallier & Polarski 2001; Linder 2003; Peebles & Ratra 2003; Dicus & Repko 2004; Wang & Mukherjee 2006). The cosmological constant is just a special case of DE, given for  $(w_0, w_a) = (-1, 0)$ , while the so called  $w$ CDM models are such that  $w_a = 0$  but  $w_0$  can take values  $\neq -1$ .

From a set of cosmological parameters, in the general case considered here given as  $\theta = \{\Omega_m, w_0, w_a\}$ , and the

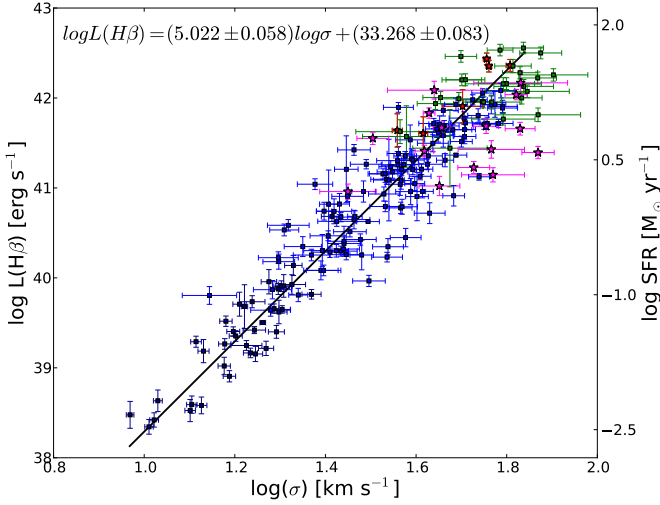


**Figure 4.**  $L - \sigma$  relation for the combined local (107 HIIG and 36 GHIIR) and high redshift (46 HIIG) samples using the [Gordon et al. \(2003\)](#) extinction curve. The fit corresponds to only the local sample of 143 objects, i.e., does not include the 46 high- $z$  HIIG. Dark blue squares: GHIIR. Blue squares: local HIIG. Pink stars: our high- $z$  MOSFIRE observations: Red stars: our high- $z$  XShooter observations ([Terlevich et al. 2015](#)). Green squares: data from the literature (see §2.3). The parameters of the fit are indicated at the top.

redshift, we can obtain the theoretical distance modulus of a source as:

$$\mu_\theta = 5 \log D_L(z, \theta) + \mu_0, \quad (25)$$

where  $\mu_0 = 42.384 - 5 \log h$  and  $h \equiv H_0/100$ . Inserting Equation 25 into Equation 12 we find after some simple algebra that:

$$\chi^2(\theta) = A(\theta) - 2B(\theta)\mu_0 + C\mu_0^2, \quad (26)$$

where,

$$\begin{aligned} A(\theta) &= \sum_{i=1}^N \frac{[\mu_o(z_i) - 5 \log D_L(z_i, \theta)]^2}{\epsilon^2}, \\ B(\theta) &= \sum_{i=1}^N \frac{\mu_o(z_i) - 5 \log D_L(z_i, \theta)}{\epsilon^2}, \\ C &= \sum_{i=1}^N \frac{1}{\epsilon^2}. \end{aligned}$$

For  $\mu_0 = B/C$ , Equation 26 has a minimum at:

$$\tilde{\chi}^2(\theta) = A(\theta) - \frac{B^2(\theta)}{C}. \quad (27)$$

Therefore, instead of using  $\chi^2$  we now minimise  $\tilde{\chi}^2$  which is independent of  $\mu_0$  and thus of the value of the Hubble constant (cf. [Nesseris & Perivolaropoulos 2005](#)).

#### 4.1.1 Constraining $\Omega_m$

Applying the method described above to the joint local and high- $z$  sample of 153 HIIG and using both of the two fitting approaches, the  $\chi^2$ -minimization procedure and the

MultiNest MCMC, we find  $\Omega_m = 0.276^{+0.066}_{-0.054}$  and  $\Omega_m = 0.290^{+0.056}_{-0.069}$  respectively under the priors shown in Table 5 and for the extinction curves of [Gordon et al. \(2003\)](#). Using the [Calzetti et al. \(2000\)](#) extinction curves we find a lower value of  $\Omega_m = 0.219^{+0.072}_{-0.057}$  (based on the  $\chi^2$ -minimization procedure). Note that the uncertainties are statistical and do not include the contribution of systematic errors.

In Figure 5 we present the Hubble diagram of our data using the [Gordon et al. \(2003\)](#) extinction curve and three different cosmologies, for comparison, as described in the inset in the figure.

It is important to underline that the difference in the value of  $\Omega_m$ , determined using the two different methods, MCMC and  $\chi^2$ -minimization, is well within  $1\sigma$  and can be attributed to the different error-weighting schemes that they employ.

It is interesting to note that the relatively large values of the reduced  $\chi^2$  of the fits, i.e.,  $\sim 1.7$  and  $\sim 1.1$ , respectively, for the two different extinction curves used (see Table 6), could well be attributed to the fact that we have not added in quadrature the systematic uncertainty in  $\mu$ . For a value  $\sim 0.22$ , added in quadrature to the Equation 15, the reduced  $\chi^2$  drops to  $\sim 1$ . One important such systematic, which is not taken into account, is related to the second parameter (size of the HII region) in the  $L - \sigma$  correlation (see for example [Chávez et al. \(2014\)](#)).

#### 4.1.2 Comparison with previous $\Omega_m$ results

The comparison of our MCMC estimated  $\Omega_m = 0.290^{+0.056}_{-0.069}$  (stat) with other literature results is summarized in Figure 6. In Planck Collaboration XVI (2014, Sect. 5.4) the light-curve parameters and covariance matrices obtained for the SiFTO light-curve model ([Conley et al. 2008](#)) lead to an  $\Omega_m$  value significantly lower than that obtained from the SALT2 ([Guy et al. 2007](#)) analysis. Interesting is the comparison of the SiFTO and SALT2 analyses obtained when the systematic uncertainties are not taken into account.

For example [Betoule et al. \(2014\)](#) find  $\Omega_m = 0.289 \pm 0.018$  (stat) that differs from the value published in ([Conley et al. 2011](#), hereafter C11) of  $\Omega_m = 0.246 \pm 0.018$  (stat) and  $\Omega_m = 0.272 \pm 0.016$  (stat) by  $2.4\sigma$  and  $1.1\sigma$  using the SALT2 and SiFTO light-curve models, respectively. The differences between SALT2 and SiFTO analyses are probably caused by different weights assigned to SNIa on the Hubble diagram rather than differences in the models. The difference is reduced by the recalibrated-reanalysis of the C11 sample by [Betoule et al. \(2014\)](#), who find  $\Omega_m = 0.291 \pm 0.022$  (stat), reducing the discrepancy between C11 and the Planck Collaboration XVI (2014) value of  $\Omega_m = 0.315 \pm 0.017$  (stat + sys).

Our determination of  $\Omega_m = 0.290^{+0.056}_{-0.069}$  (stat) is in agreement with the SNIa measurements of  $\Omega_m = 0.289 \pm 0.018$  (stat), based on 740 SNIa ([Betoule et al. \(2014\)](#)), and of  $\Omega_m = 0.277^{+0.022}_{-0.021}$  (stat), based on the 580 SNIa of the Union 2.1 sample ([Suzuki et al. \(2012\)](#)), where the highest redshift is 1.415. Our value is also consistent with the most recent CMB measurement from WMAP9 ([Bennett et al. 2013](#)), which provides a value of  $\Omega_m = 0.279 \pm 0.025$ , as well as with the Planck Collaboration measurement (2016a; 2016b; 2018) of  $\Omega_m = 0.308 \pm 0.012$ ;  $\Omega_m = 0.320 \pm 0.009$

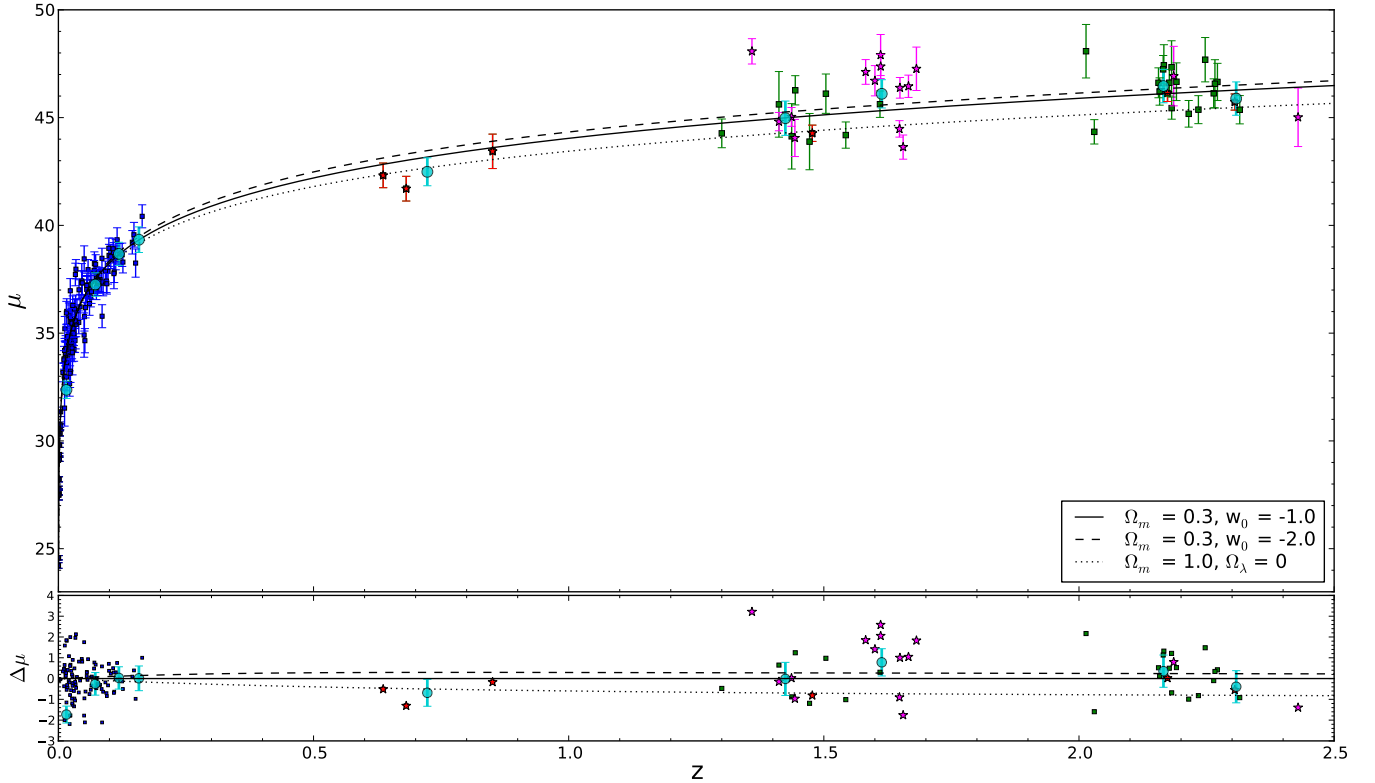


**Figure 5.** Hubble-Lemaitre diagram connecting our local and high redshift samples up to  $z \sim 2.5$  for three different cosmologies shown in the inset. Dark blue squares: GHIIR; blue squares: local HIIG; pink stars: our high- $z$  MOSFIRE observations; red stars: our high- $z$  XShooter observations; green squares: data from the literature and sky blue circles: the mean in redshift bins. Residuals are plotted in the bottom panel. Note the huge dynamical range covered by the distance modulus with a single distance estimator ( $L - \sigma$ ).

**Table 5.** Priors for Constrained Parameters.

Parameter	Prior
Cosmological Parameters	
$h$	Uniform [0.5, 1.0]
$\Omega_m$	Uniform [0.0, 1.0]
$w_0$	Uniform [-2.0, 0.0]
$w_a$	Uniform [-4.0, 2.0]
$w_b$	Uniform [0.0, 0.05]
HIIG Nuisance Parameters	
$\alpha$	Uniform [25.0, 35.0]
$\beta$	Uniform [0.0, 8.0]
SNIa Nuisance Parameters	
$\alpha$	Uniform [0.0, 0.3]
$\beta$	Uniform [2.0, 4.0]
$M_B^1$	Uniform [-18.0, -21.0]
$\Delta_M$	Uniform [-2.0, 0.0]

and  $\Omega_m = 0.315 \pm 0.007$  respectively, where both statistical and systematic uncertainties are included.

#### 4.1.3 Comparison with previous results in the $\{\Omega_m, w_0\}$ plane

We compare our current with our previous results in the  $\{\Omega_m, w_0\}$  plane (Terlevich et al. 2015; Chávez et al. 2016), based on the  $\chi^2$ -minimization procedure, in Figure 7 and in Table 6.

Figure 7 shows the  $1\sigma$  and  $2\sigma$  confidence levels in the  $\{\Omega_m, w_0\}$  plane based on the  $\chi^2$ -minimization procedure, for the  $L - \sigma$  parameters corresponding to the Calzetti et al. (2000) (dashed contours) and the Gordon et al. (2003) (continuous contours) extinction correction curves, for which we obtain  $\Omega_m, w_0 = \{0.201^{+0.120}_{-0.084}, -0.926^{+0.303}_{-0.450}\}$  and  $\{0.249^{+0.105}_{-0.081}, -0.887^{+0.264}_{-0.384}\}$ , respectively. Values are listed in Table 6.

The addition of just 15 new high- $z$  HIIG to the sample presented in our previous work (cf. Chávez et al. 2016) has produced a significant improvement, exemplified by the fact that now we obtain  $\{\Omega_m, w_0\}$  central values that are in agreement with other analyses and with errors that are reasonably small considering the modest size of our high- $z$  HIIG sample.

Figure 8 and Table 6 show the MCMC  $\{\Omega_m, w_0\}$  constraints based on our sample of 153 HIIG using the priors shown in Table 5. When we constrain the  $\{\Omega_m, w_0\}$  plane,

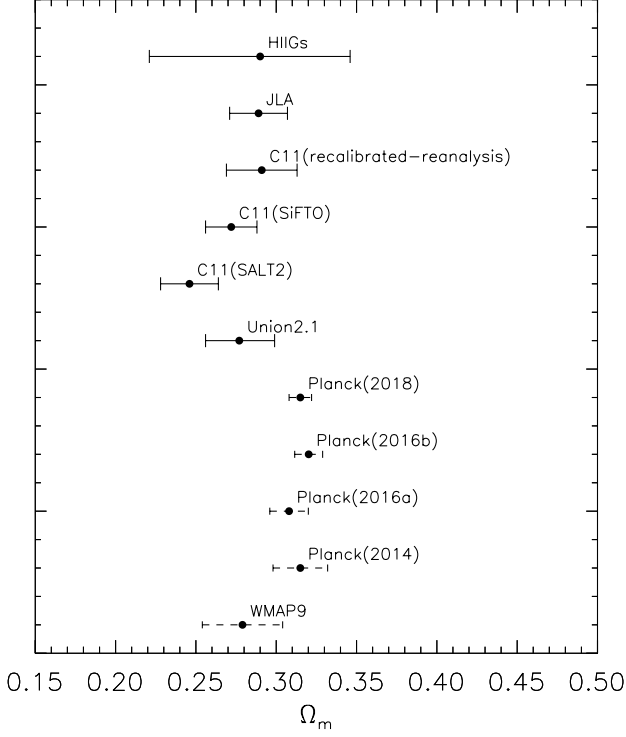


**Figure 6.** Comparison of the result of this work with the most recent estimates of  $\Omega_m$  from the literature. The dashed error bars include statistical + systematic uncertainties and the continuous error bars, only statistical uncertainties. Our result for  $\Omega_m$  is in the top line.

we obtain  $\Omega_m = 0.280^{+0.130}_{-0.100}$  and  $w_0 = -1.12^{+0.58}_{-0.32}$  (stat). Our results are in agreement, within  $1\sigma$ , with the SNIa measurements of  $\{\Omega_m, w_0\} = \{0.281^{+0.067}_{-0.092}, -1.011^{+0.208}_{-0.231}\}$  (stat), based on the Union 2.1 sample of 580 SNIa (Suzuki et al. (2012)) and of  $\{0.350 \pm 0.035, -1.251 \pm 0.144\}$  (stat), based on the most recent sample of 1048 SNIa (Scolnic et al. (2018)). The smaller uncertainties in the SNIa based results reflect the much larger samples, i.e., 580 and 1048 SNIa versus 153 HIIG.

#### 4.1.4 HII galaxies and GHIIR simultaneous constraints

Using simultaneously GHIIR and HIIG data, a global fit of all the free parameters, nuisance and cosmological, provides the following results  $\alpha = 33.20 \pm 0.14$ ,  $\beta = 5.06 \pm 0.12$ ,  $h = 0.706 \pm 0.040$ ,  $\Omega_m = 0.363^{+0.16}_{-0.081}$  and  $w_0 = -1.03^{+0.62}_{-0.33}$ ; while in Figure 9 we plot the  $1\sigma$  and  $2\sigma$  contours in various planes.

Remarkably, although the errors are quite large, the corresponding mean values are in excellent agreement with those of Scolnic et al. (2018). This confirms our proposal that the Hubble relation based on the HIIG could provide an efficient tool to understand the mechanism of late (dark energy) cosmic acceleration. We argue that new data from

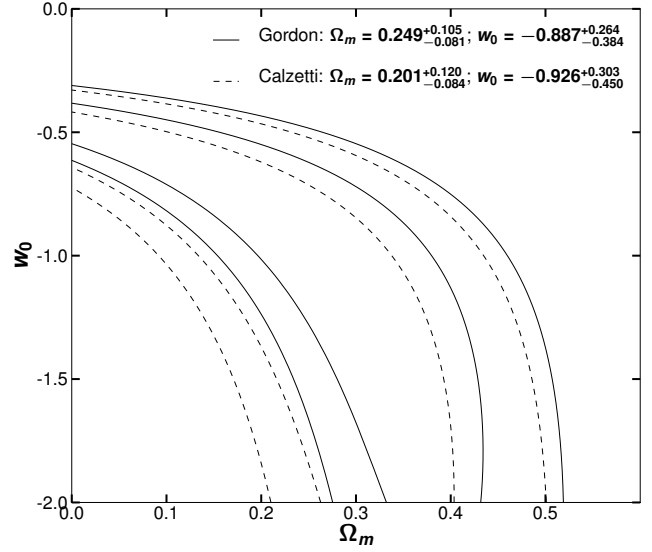


**Figure 7.**  $\chi^2$  likelihood contours for  $\Delta\chi^2 = \chi^2_{tot} - \chi^2_{tot,min}$  equal to 2.30 and 6.17 corresponding to the  $1\sigma$  and  $2\sigma$  confidence levels in the  $\{\Omega_m, w_0\}$  plane for our 153 HIIG at intermediate and high redshift. a) solid line: Gordon et al. (2003) extinction correction ( $\alpha = 33.268 \pm 0.083$  and  $\beta = 5.022 \pm 0.058$ ), b) dotted line: Calzetti et al. (2000) extinction correction ( $\alpha = 33.11 \pm 0.145$  and  $\beta = 5.05 \pm 0.097$ ).

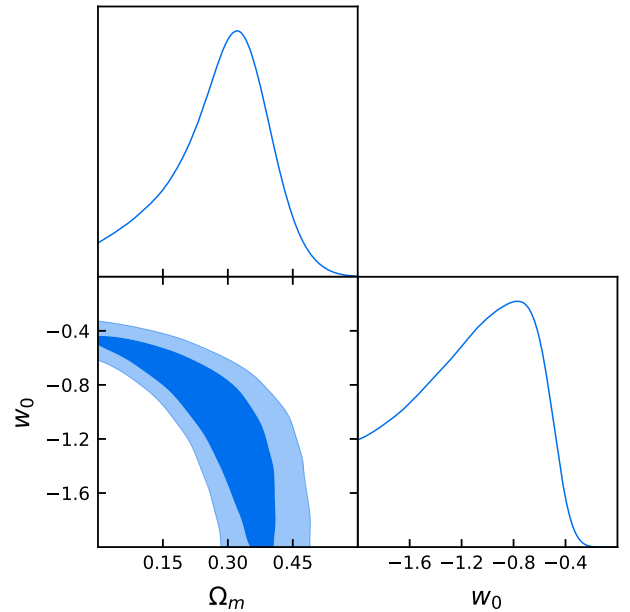


**Figure 8.** Likelihood contours corresponding to the  $1\sigma$  and  $2\sigma$  confidence levels in the  $\{\Omega_m, w_0\}$  space for the HIIG sample corrected for extinction with Gordon et al. (2003). The distance estimator parameters are:  $\alpha = 33.268 \pm 0.083$  and  $\beta = 5.022 \pm 0.058$ .

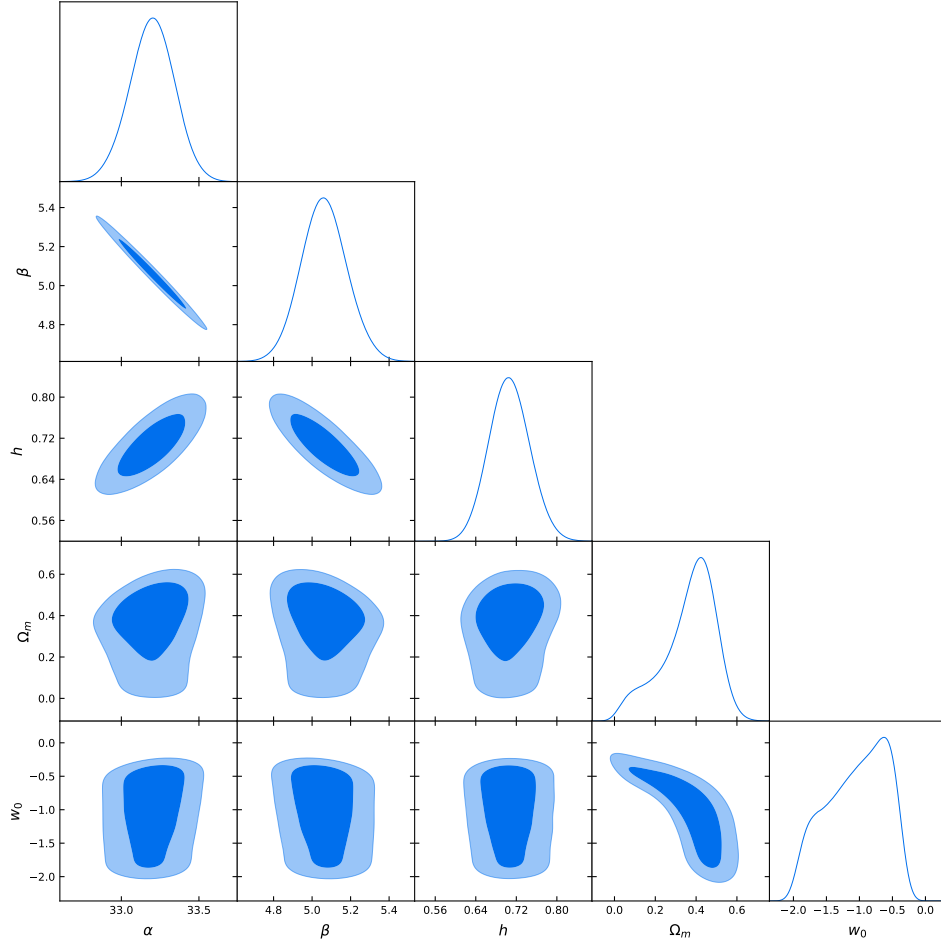


**Figure 9.** Likelihood contours corresponding to the  $1\sigma$  and  $2\sigma$  confidence levels in the  $\{\alpha, \beta, h, \Omega_m, w_0\}$  space for the HIIG sample corrected for extinction with [Gordon et al. \(2003\)](#). The resulting constraints are  $\{\alpha, \beta, h, \Omega_m, w_0\} = \{33.20 \pm 0.14, 5.06 \pm 0.12, 0.706 \pm 0.040, 0.363^{+0.16}_{-0.081}, -1.03^{+0.62}_{-0.33}\}$ .

VLT/KMOS (González-Morán et al. in preparation) and from GTC/MEGARA (at present in an observing queue) will allow us to measure the DE EoS parameter as well as to check whether  $w$  depends on time.

## 4.2 CMB constraints

The information about the position of the acoustic peaks of the CMB, can be quantified by three observables:  $\{l_a, R, \omega_b\}$ , where  $l_a$  is the acoustic scale related to the comoving sound speed horizon,  $R$  is the shift parameter ([Bond et al. 1997](#); [Nesseris & Perivolaropoulos 2007](#)), the ratio of the position of the first peak to that of a reference model, and

$$\omega_b \equiv \Omega_b h^2, \quad (28)$$

where  $\Omega_b$  is the current baryon density parameter. The first two quantities are related to the angular diameter distance, which in flat space can be given by:

$$d_A(z, \theta) = \frac{c}{H_0} \frac{1}{1+z} \int_0^z \frac{dz'}{E(z', \theta)} \quad (29)$$

and to the comoving sound speed horizon:

$$r_s(z, \theta) = \frac{c}{H_0} \int_0^{1/(1+z)} da \frac{c_s(a)}{a^2 E(a)}, \quad (30)$$

where  $c_s(a)$  is the sound speed of the baryon-photon fluid before recombination:

$$c_s(a) = \frac{1}{\sqrt{3 + 3(3\Omega_b/4\Omega_\gamma)a}}, \quad (31)$$

where  $\Omega_\gamma$  is the current photon energy density parameter.

The acoustic scale is given by:

$$l_a = (1+z_*) \frac{\pi d_A(z_*, \theta)}{r_s(z_*, \theta)}, \quad (32)$$

the shift parameter can be given as:

$$R(\theta) = \sqrt{\Omega_m} \int_0^{z_*} \frac{dz}{E(z, \theta)}, \quad (33)$$

and  $z_*$  is given by the fitting formula of [Hu & Sugiyama \(1996\)](#):

$$z_* = 1048[1 + 0.00124(\Omega_b h^2)^{-0.738}][1 + g_1(\Omega_m h^2)^{g_2}], \quad (34)$$

$$g_1 = \frac{0.0783(\Omega_b h^2)^{-0.238}}{1 + 39.5(\Omega_b h^2)^{0.763}}, \quad (35)$$

$$g_2 = \frac{0.560}{1 + 21.1(\Omega_b h^2)^{1.81}}. \quad (36)$$

In Chávez et al. (2016) we used only the measured shift parameter, according to Planck data (Shafer & Huterer 2014) as  $R = 1.7499 \pm 0.0088$  at the redshift of decoupling (i.e., at the last scattering surface). Here we use updated values for  $\{l_a, R, \omega_b\}$  derived from the Planck 2015 likelihoods assuming a flat Universe (Planck Collaboration et al. 2016a). The parameters values derived from observations are given by cf. Wang & Dai (2016):

$$\begin{aligned} \mathbf{P}_o &= \{l_a, R, \omega_b\} \\ &= \{301.77 \pm 0.09, 1.7482 \pm 0.0048, 0.02226 \pm 0.00016\}, \end{aligned} \quad (37)$$

with an inverse covariance matrix,  $\mathbf{C}^{-1}$ , given as:

$$\begin{bmatrix} 1.47529862\text{e}+02 & -9.50243997\text{e}+02 & 6.75330855\text{e}+03 \\ -9.49518029\text{e}+02 & 8.87656028\text{e}+04 & 1.66515286\text{e}+06 \\ 6.78491359\text{e}+03 & 1.66491606\text{e}+06 & 7.46953427\text{e}+07 \end{bmatrix}$$

The final likelihood function is:

$$\mathcal{L}_{CMB} \propto \exp \left[ -\frac{1}{2} \Delta \mathbf{C}^{-1} \Delta^\dagger \right], \quad (38)$$

where,  $\Delta = \mathbf{P}_\theta - \mathbf{P}_o$ , and  $\mathbf{P}_\theta = \{l_a, R, \omega_b\}$  is the vector of modeled parameters as described in Equations 32, 33 and 28; likewise  $\mathbf{C}^{-1}$  is the inverse of the corresponding covariance matrix and  $\Delta^\dagger$  the transpose of  $\Delta$ .

In Table 6 we show the maximum likelihood results for the plane  $\{\Omega_m, w_0, w_b\}$  using the updated values of  $\{l_a, R, \omega_b\}$  as described above. For the parameter modeling we use a value of  $h = 0.6774$ , which is consistent with Planck latest determination (Planck Collaboration et al. 2016a). We use the MultiNest algorithm with the priors listed in Table 5 to calculate the probability distribution.

### 4.3 BAO Constraints

The Baryonic Acoustic Oscillation (BAO) scale, is a feature produced in the last scattering surface by the competition between the pressure of the coupled baryon-photon fluid and gravity. The resulting sound waves leave an overdensity signature at a certain length scale of the matter distribution. This length scale is related to the comoving distance that a sound wave can travel until recombination and in practice it manifests itself as a feature in the correlation function of galaxies on large scales ( $\sim 100 h^{-1}$  Mpc). In recent years, measurements of BAOs have proven to be an extremely useful “standard ruler”. The BAOs were clearly identified, for the first time, as an excess in the clustering pattern of the SDSS luminous red galaxies (Eisenstein et al. 2005) and of the 2dFGRS galaxies (Cole et al. 2005). Since then a large number of dedicated surveys have been used to measure BAOs, among which the WiggleZ Dark Energy Survey (Blake et al. 2011), the 6dFGS (Beutler et al. 2011) and the SDSS Baryon Oscillation Spectroscopic Survey (BOSS) of SDSS-III (Eisenstein et al. 2011; Anderson et al. 2014; Aubourg et al. 2015).

Here we use BAOs measurements from the Reconstructed 6-degree Field Galaxy Survey (Carter et al. 2018),

the WiggleZ Dark Energy Survey (Kazin et al. 2014) and the SDSS-III Baryon Oscillation Spectroscopic Survey (Gil-Marín et al. 2016) as compiled in Anagnostopoulos et al. (2019, see the first six data points in their Table III), which following their notation, is given in terms of the parameter  $\lambda(z_i, \theta)$  defined as:

$$\lambda(z_i, \theta) = \begin{cases} d_V r_{d, fid} / r_d, & 1 \leq i \leq 4 \\ d_A / r_d, & 5 \leq i \leq 6 \end{cases}$$

with  $z_i$  the redshift at which the signature of the acoustic oscillations has been measured and

$$d_A = \frac{d_L(z, \theta)}{(1+z)^2}, \quad (39)$$

$$d_V = \left[ \frac{cd_A^2 z(1+z)^2}{H(z, \theta)} \right]^{1/3}, \quad (40)$$

additionally,  $r_d$  is the standard ruler, which in  $\Lambda$ CDM cosmology is equal to the comoving sound horizon  $r_s$  as given in Equation 30.

The corresponding likelihood function is given by:

$$\mathcal{L}_{BAO} \propto \exp \left[ -\frac{1}{2} \Delta \mathbf{C}^{-1} \Delta^\dagger \right]. \quad (41)$$

where,  $\Delta = \mathbf{P}_{z, \theta} - \mathbf{P}_o$ , is the difference between the vector of modeled parameters,  $\mathbf{P}_{z, \theta} = \{\lambda(z_1, \theta), \dots, \lambda(z_{10}, \theta)\}$ , as defined above, and the vector of observed data,  $\mathbf{P}_o = \{\lambda(z_1)_o, \dots, \lambda(z_{10})_o\}$ .

The constraints for BAOs, using the MCMC MultiNest algorithm, a value of  $h = 0.6774$  and the priors shown in Table 5 in the plane  $\{\Omega_m, w_0\}$ , are given in Table 6.

### 4.4 Type Ia Supernovae Constraints

For SNIa we apply a similar methodology where the likelihood function is given as:

$$\mathcal{L}_{SNIa} \propto \exp \left[ -\frac{1}{2} (\mu_o - \mu_m(z|\theta)) \mathbf{C}^{-1} (\mu_o - \mu_m(z|\theta))^\dagger \right], \quad (42)$$

where  $\mathbf{C}$  is the covariance matrix of  $\mu_o = m_B^* - (M_B - \alpha X_1 + \beta C)$ , with  $m_B^*$  the observed peak magnitude in the rest-frame  $B$  band and  $\alpha$ ,  $\beta$  and  $M_B$  are nuisance parameters. It has been shown that the absolute magnitude  $M_B$  and the parameter  $\beta$  depend on the host galaxy parameters (Sullivan et al. 2011; Johansson et al. 2013). Following Betoule et al. (2014) we parametrize this dependence as:

$$M_B = \begin{cases} M_B^1 & \text{if } M_* < 10^{10} M_\odot \\ M_B^1 + \Delta_M & \text{otherwise} \end{cases}$$

We analyze the JLA compilation of 740 SNIa presented in Betoule et al. (2014). We show constraints in the parameter space  $\{\alpha, \beta, M_B^1, \Delta_M, \Omega_m, w_0\}$  in Table 6 where  $\{\alpha, \beta, M_B^1, \Delta_M\}$  are nuisance parameters, following Betoule et al. (2014) we use a fiducial value of  $h = 0.7$  for the analysis. These constraints have been calculated using the MCMC MultiNest algorithm with the priors shown in Table 5.

### 4.5 Joint analysis

With a view to place tighter constraints on the parameter space of the DE EoS, the different cosmological probes described above were combined through a joint likelihood

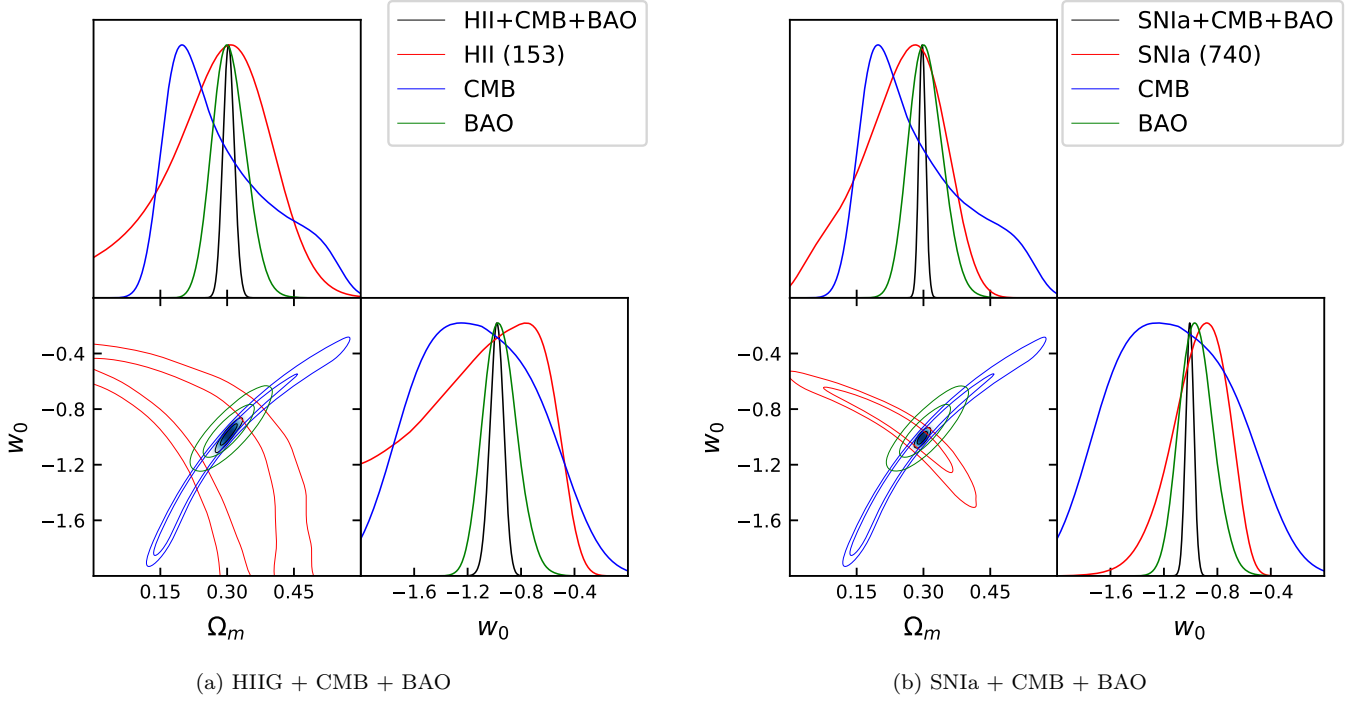


**Figure 10.** Likelihood contours corresponding to the  $1\sigma$  and  $2\sigma$  confidence levels in the  $\{\Omega_m, w_0\}$  space for a) the joint sample of HIIG, CMB(Wang & Dai 2016) and BAO(Anagnostopoulos et al. 2019) and b) the joint sample of SNIa(JLA Betoule et al. 2014), CMB and BAO. For HIIG and SNIa we show the number of objects used in the analysis in parentheses at the inset. Only statistical uncertainties are shown.

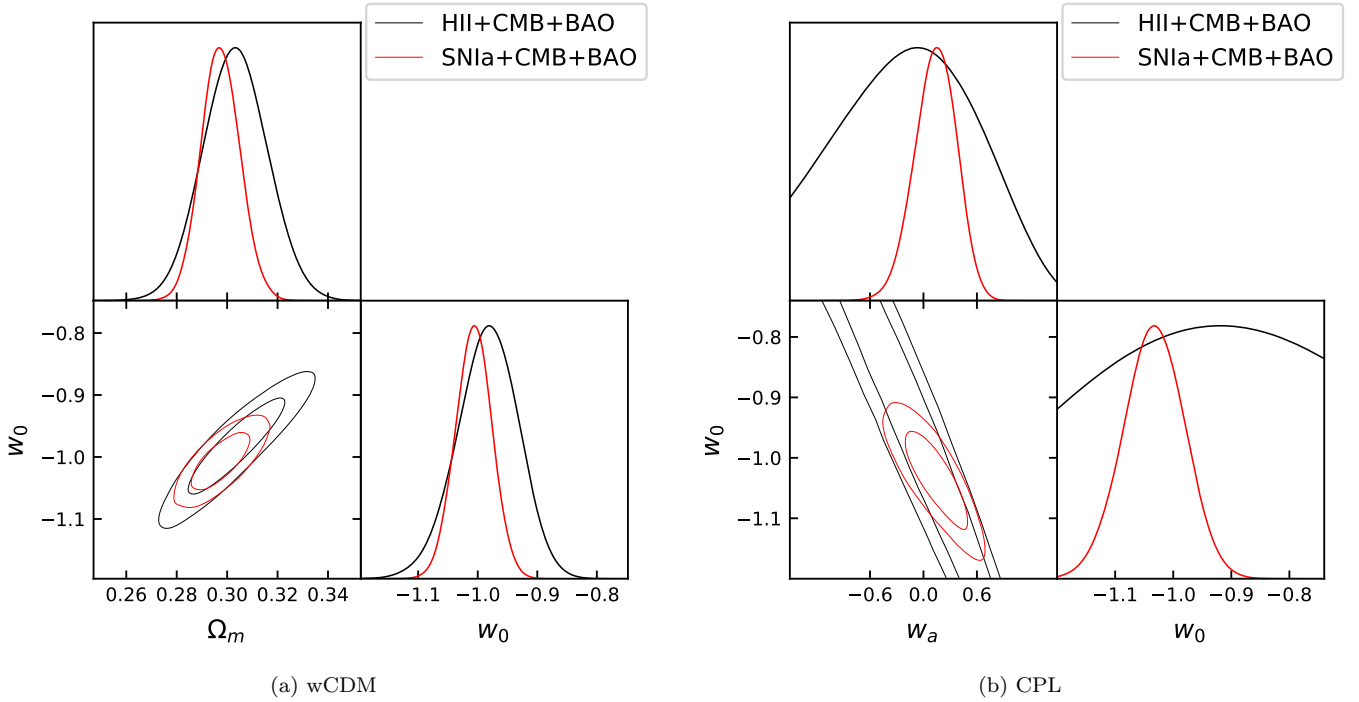


**Figure 11.** Comparison of the joint likelihood contours of the HIIG/CMB/BAO (black contours) and of the SNIa/CMB/BAO (red contours) probes. Left-hand panel:  $w$ CDM DE EoS parametrization ( $\{h, \Omega_m, w_0\}$ ). Right-hand panel: CPL DE EoS parametrization ( $\{h, \Omega_m, w_0, w_a\}$ ).

analysis given by the product of the individual likelihoods according to:

$$\mathcal{L}_{Tot}(\theta) = \prod_{i=1}^n \mathcal{L}_i(\theta) \quad (43)$$

where  $n$  is the total number of cosmological probes used<sup>4</sup>.

In Figure 10 panel (a) we show the joint analysis for HIIG (with Gordon et al. 2003, extinction correction), CMB and BAOs; in panel (b) the joint analysis for SNIa, CMB and BAOs for the space  $\{\Omega_m, w_0\}$ . In Table 6 we also show the results for the space  $\{\Omega_m, w_0, w_a\}$ . In all cases the solutions are calculated using the MCMC MultiNest algorithm with the priors shown in Table 5.

From Figure 10 and Table 6 it is clear that the solution space of HIIG/CMB/BAO, although less constrained, is certainly compatible with the solution space of SNIa/CMB/BAO, which also can be appreciated from the results shown in Table 6.

In Figure 11 we show the joint likelihood contours for HIIG/BAO/CMB (black contours) and SNIa/BAO/CMB (red contours) probes for  $\Lambda$ CDM and CPL DE EoS parametrizations. It is clear that, for both parametrizations, the HIIG/BAO/CMB and SNIa/BAO/CMB joint probes agree with each other although the later produces better constraints, which is expected given the much larger number of SNIa (740) compared with the number of HIIG (153) analyzed.

## 5 CONCLUSIONS.

We have used the  $L - \sigma$  distance indicator for HIIG to derive independently cosmological parameters. To this end, we present observations of a sample of 25 HIIG in the redshift range  $1.3 \leq z \leq 2.5$  obtained with the Keck-MOSFIRE spectrograph of which 15 were selected for this work. These were combined with another 6 high- $z$  galaxies observed by us with VLT-XShooter (Terlevich et al. 2015) and a compilation of 25 more objects from the literature. In total, we use the data for 46 high redshift and 107 local HIIG (Chávez et al. 2014), making a grand total of 153 HIIG covering the redshift range  $0.01 \leq z \leq 2.5$ . From the analysis of these data we have found the following:

1 - Using two fitting approaches, the  $\chi^2$ -minimization procedure and the MultiNest MCMC, we find  $\Omega_m = 0.276^{+0.066}_{-0.054}$  and  $\Omega_m = 0.290^{+0.056}_{-0.069}$  (stat) respectively, applying to the data the extinction curve of Gordon et al. (2003). The values of  $\Omega_m$ , determined using the two fitting approaches are within  $1\sigma$  being the difference probably related to the dissimilar error-weighting schemes that the two fittings methods employ.

2 - The constraints in  $\Omega_m$  provided by the HIIG probe are shown to be consistent, although with larger errors, with those of the SNIa (Suzuki et al. 2012) of  $\Omega_m = 0.277^{+0.022}_{-0.021}$  (stat) for the Union 2.1 sample of 580 SNIa and with (Betoule et al. 2014) of  $\Omega_m = 0.289 \pm 0.018$

(stat) for 740 SNIa that took more than a decade to compile.

3 - To facilitate the comparison with our previous work (cf. Terlevich et al. 2015; Chávez et al. 2016) based on the  $\chi^2$ -minimization procedure, we present our results using the Calzetti et al. (2000) extinction curve, finding  $\Omega_m, w_0 = \{0.201^{+0.120}_{-0.084}, -0.926^{+0.303}_{-0.450}\}$ , which have produced a significant improvement since now we obtain  $\{\Omega_m, w_0\}$  central values that are in agreement with other analysis and with errors that are reasonably small considering the modest increase of the sample by the inclusion of 15 new high- $z$  HIIG.

4 - The constraints in the  $\{\Omega_m, w_0\}$  plane provided by the HIIG are  $\Omega_m = 0.280^{+0.130}_{-0.100}$  and  $w_0 = -1.12^{+0.58}_{-0.32}$  (stat) using the Gordon et al. (2003) extinction curve. These are in agreement with the values obtained by Suzuki et al. (2012):  $\Omega_m = 0.281^{+0.067}_{-0.092}$  and  $w_0 = -1.011^{+0.208}_{-0.231}$  (stat) for the Union 2.1 sample.

5 - A global fit of all the free parameters using simultaneously GHIIR and HIIG data provides the following results  $\alpha = 33.20 \pm 0.14$ ,  $\beta = 5.06 \pm 0.12$ ,  $h = 0.706 \pm 0.040$ ,  $\Omega_m = 0.363^{+0.16}_{-0.081}$  and  $w_0 = -1.03^{+0.62}_{-0.33}$ . Although the errors are relatively large, the corresponding mean values are in excellent agreement with those of the most recent SNIa work by Scolnic et al. (2018)  $\Omega_m = 0.350 \pm 0.035$  and  $w_0 = -1.251 \pm 0.144$  (stat) for a sample of 1048 SNIa.

6 - The joint HIIG analysis with other cosmological probes (CMB and BAOs) further test the effectiveness of using HIIG as tracers of the Hubble expansion. This analysis reduces dramatically the solution space in comparison with our previous results, providing quite stringent constraints on the  $\{\Omega_m, w_0\}$  plane.

7 - In order to test the consistency of the derived cosmological constraints using HIIG compared with those of SNIa, we show the joint likelihood contours for HIIG/BAO/CMB and SNIa/BAO/CMB probes for  $\Lambda$ CDM and CPL DE EoS parametrizations. It is clear that, for both parametrizations, the HIIG/BAO/CMB and SNIa/BAO/CMB joint probes are in agreement with each other, although the later produces better constraints, which is expected given the much larger number of SNIa (740) compared with the number of HIIG (153) analysed.

It is very encouraging that even with the current small number of HIIG and after a total of only 7 observing nights, our analysis provides independent constraints on the cosmological parameters, which are in agreement with those of SNIa. This confirms our proposal that the Hubble relation for HIIG could provide an efficient tool to understand the mechanism of late cosmic acceleration.

## ACKNOWLEDGEMENTS

The authors wish to recognize and acknowledge the very significant cultural role and reverence that the summit of Maunakea has always had within the indigenous Hawaiian community. We are most fortunate to have the opportunity

<sup>4</sup> Likelihoods are normalised to their maximum values.

**Table 6.** Results obtained for the different samples and their combinations, only statistical uncertainties are considered. Values in parenthesis have been left fixed. Results for both extinction corrections are shown for the HIIG; (c) Calzetti et al. (2000) extinction correction ( $\alpha = 33.11 \pm 0.145$  and  $\beta = 5.05 \pm 0.097$ ) or (g) Gordon et al. (2003) extinction correction ( $\alpha = 33.268 \pm 0.083$  and  $\beta = 5.022 \pm 0.058$ ).

Samples	$\alpha$	$\beta$	$M_B^1$	$\Delta_M$	$\omega_b$	$h$	$\Omega_m$	$w_0$	$w_a$	N	$\chi^2$
HIIG <sub>c</sub> (ChiSq)	—	—	—	—	—	—	$0.219^{+0.072}_{-0.057}$	(-1.0)	(0.0)	153	171.35
HIIG <sub>c</sub> (ChiSq)	—	—	—	—	—	—	$0.201^{+0.120}_{-0.084}$	$-0.926^{+0.303}_{-0.450}$	(0.0)	153	171.34
HIIG <sub>g</sub> (ChiSq)	—	—	—	—	—	—	$0.276^{+0.066}_{-0.054}$	(-1.0)	(0.0)	153	256.22
HIIG <sub>g</sub> (ChiSq)	—	—	—	—	—	—	$0.249^{+0.105}_{-0.081}$	$-0.887^{+0.264}_{-0.384}$	(0.0)	153	256.19
HIIG <sub>g</sub> (MCMC)	—	—	—	—	—	—	$0.290^{+0.056}_{-0.069}$	(-1.0)	(0.0)	153	254.99
HIIG <sub>g</sub> (MCMC)	—	—	—	—	—	—	$0.280^{+0.130}_{-0.100}$	$-1.12^{+0.58}_{-0.52}$	(0.0)	153	255.14
CMB	—	—	—	—	$0.02225 \pm 0.00016$	(0.6774)	$0.3107 \pm 0.0029$	$-0.954^{+0.020}_{-0.018}$	(0.0)	3	0.02
BAO	—	—	—	—	(0.02225)	(0.6774)	$0.306^{+0.034}_{-0.041}$	$-0.95^{+0.12}_{-0.14}$	(0.0)	6	1.76
SNla	$0.1411 \pm 0.0064$	$3.148 \pm 0.077$	$-19.041 \pm 0.017$	$-0.060 \pm 0.012$	—	(0.7)	$0.247^{+0.11}_{-0.064}$	$-0.94^{+0.23}_{-0.16}$	(0.0)	740	724.38
HIIG <sub>c</sub> +CMB+BAO	—	—	—	—	(0.02225)	$0.686 \pm 0.015$	$0.303 \pm 0.013$	$-0.983^{+0.054}_{-0.048}$	(0.0)	162	257.53
HIIG <sub>g</sub> +CMB+BAO	—	—	—	—	(0.02225)	$0.681 \pm 0.025$	$0.309^{+0.021}_{-0.024}$	$-0.88^{+0.30}_{-0.34}$	$-0.36^{+1.1}_{-0.73}$	162	257.56
SNla+CMB+BAO	$0.1407 \pm 0.0072$	$3.265 \pm 0.088$	—	$-0.064 \pm 0.014$	(0.02225)	$0.6930 \pm 0.0086$	$0.2975 \pm 0.0077$	$-1.007 \pm 0.031$	(0.0)	749	589.61
SNla+CMB+BAO	$0.1411 \pm 0.0072$	$3.270 \pm 0.088$	—	$-0.063 \pm 0.014$	(0.02225)	$0.690 \pm 0.011$	$0.3001 \pm 0.0090$	$-1.033 \pm 0.053$	$0.13^{+0.25}_{-0.22}$	749	589.25

to conduct observations from this mountain. ALGM and RC are grateful to the Mexican Research Council (CONACYT) for supporting this research under studentship 419392 and under grant 263561, respectively. ALGM is also grateful to Luca Ricci, support astronomer of the Keck Telescope, for his help during the observations and data reduction. RT, ET, MP and SB are grateful to the Kavli Institute for Cosmology in Cambridge for its hospitality during a visit in March that allowed us to conclude this work.

## REFERENCES

- Amanullah R., et al., 2010, *ApJ*, **716**, 712
- Anagnostopoulos F. K., Basilakos S., Kofinas G., Zarikas V., 2019, *Journal of Cosmology and Astro-Particle Physics*, 2019, 053
- Anderson L., et al., 2014, *MNRAS*, **441**, 24
- Aubourg É., et al., 2015, *Phys. Rev. D*, **92**, 123516
- Belli S., Newman A. B., Ellis R. S., 2014, *ApJ*, **783**, 117
- Bennett C. L., et al., 2013, *ApJS*, **208**, 20
- Betoule M., et al., 2014, *A&A*, **568**, A22
- Beutler F., et al., 2011, *MNRAS*, **416**, 3017
- Blake C., et al., 2011, *MNRAS*, **418**, 1707
- Bond J. R., Efstathiou G., Tegmark M., 1997, *MNRAS*, **291**, L33
- Brammer G. B., et al., 2012, *ApJ*, **758**, L17
- Bruce V. A., et al., 2012, *MNRAS*, **427**, 1666
- Calzetti D., Armus L., Bohlin R. C., Kinney A. L., Koornneef J., Storchi-Bergmann T., 2000, *ApJ*, **533**, 682
- Carter P., Beutler F., Percival W. J., Blake C., Koda J., Ross A. J., 2018, *MNRAS*, **481**, 2371
- Chávez R., Terlevich E., Terlevich R., Plionis M., Bresolin F., Basilakos S., Melnick J., 2012, *MNRAS*, **425**, L56
- Chávez R., Terlevich R., Terlevich E., Bresolin F., Melnick J., Plionis M., Basilakos S., 2014, *MNRAS*, **442**, 3565
- Chávez R., Plionis M., Basilakos S., Terlevich R., Terlevich E., Melnick J., Bresolin F., González-Morán A. L., 2016, *MNRAS*, **462**, 2431
- Chevallier M., Polarski D., 2001, *International Journal of Modern Physics D*, **10**, 213
- Cirasuolo M., et al., 2007, *MNRAS*, **380**, 585
- Cole S., et al., 2005, *MNRAS*, **362**, 505
- Conley A., et al., 2008, *ApJ*, **681**, 482
- Conley A., et al., 2011, *ApJS*, **192**, 1
- Cooray A., et al., 2011, preprint, ([arXiv:1110.3784](https://arxiv.org/abs/1110.3784))
- Dicus D. A., Repko W. W., 2004, *Phys. Rev. D*, **70**, 083527
- Eisenstein D. J., et al., 2005, *ApJ*, **633**, 560
- Eisenstein D. J., et al., 2011, *AJ*, **142**, 72
- Elias J. H., Frogel J. A., Matthews K., Neugebauer G., 1982, *AJ*, **87**, 1029
- Erb D. K., Steidel C. C., Shapley A. E., Pettini M., Reddy N. A., Adelberger K. L., 2006a, *ApJ*, **646**, 107
- Erb D. K., Steidel C. C., Shapley A. E., Pettini M., Reddy N. A., Adelberger K. L., 2006b, *ApJ*, **647**, 128
- Fernández Arenas D., et al., 2018, *MNRAS*, **474**, 1250
- Feroz F., Hobson M. P., 2008, *MNRAS*, **384**, 449
- Feroz F., Hobson M. P., Bridges M., 2009, *MNRAS*, **398**, 1601
- Feroz F., Hobson M. P., Cameron E., Pettitt A. N., 2013, preprint, ([arXiv:1306.2144](https://arxiv.org/abs/1306.2144))
- Freedman W. L., Madore B. F., Scowcroft V., Burns C., Monson A., Persson S. E., Seibert M., Rigby J., 2012, *ApJ*, **758**, 24
- García-Díaz M. T., Henney W. J., López J. A., Doi T., 2008, *Revista Mexicana de Astronomía y Astrofísica*, **44**, 181
- Giavalisco M., et al., 2004, *ApJ*, **600**, L93
- Gil-Marín H., et al., 2016, *MNRAS*, **460**, 4188
- Gordon K. D., Clayton G. C., Misselt K. A., Landolt A. U., Wolff M. J., 2003, *ApJ*, **594**, 279
- Grogin N. A., et al., 2011, *ApJS*, **197**, 35
- Guy J., et al., 2007, *A&A*, **466**, 11
- Hicken M., Wood-Vasey W. M., Blondin S., Challis P., Jha S., Kelly P. L., Rest A., Kirshner R. P., 2009, *ApJ*, **700**, 1097
- Hu W., Sugiyama N., 1996, *ApJ*, **471**, 542
- Jaffe A. H., et al., 2001, *Physical Review Letters*, **86**, 3475
- Johansson J., et al., 2013, *MNRAS*, **435**, 1680
- Kazin E. A., et al., 2014, *MNRAS*, **441**, 3524
- Koekemoer A. M., et al., 2007, *ApJS*, **172**, 196
- Koekemoer A. M., et al., 2011, *ApJS*, **197**, 36
- Krogager J.-K., Zirm A. W., Toft S., Man A., Brammer G., 2014, *ApJ*, **797**, 17
- Lawrence A., et al., 2007, *MNRAS*, **379**, 1599
- Leitherer C., et al., 1999, *ApJS*, **123**, 3
- Linder E. V., 2003, *Physical Review Letters*, **90**, 091301
- Lundgren B. F., et al., 2012, *ApJ*, **760**, 49
- Mancini C., et al., 2011, *ApJ*, **743**, 86
- Maseda M. V., et al., 2013, *ApJ*, **778**, L22
- Maseda M. V., et al., 2014, *ApJ*, **791**, 17
- Masters D., et al., 2014, *ApJ*, **785**, 153
- McLean I. S., et al., 2010, in *Ground-based and Airborne Instrumentation for Astronomy III*. pp 77351E–77351E–12, [doi:10.1117/12.856715](https://doi.org/10.1117/12.856715)
- McLean I. S., et al., 2012, in *Ground-based and Airborne Instrumentation for Astronomy IV*. p. 84460J, [doi:10.1117/12.924794](https://doi.org/10.1117/12.924794)

- Melnick J., Terlevich R., Terlevich E., 2000, *MNRAS*, **311**, 629  
Melnick J., et al., 2017, *A&A*, **599**, A76  
Nesseris S., Perivolaropoulos L., 2005, *Phys. Rev. D*, **72**, 123519  
Nesseris S., Perivolaropoulos L., 2007, *JCAP*, **1**, 18  
Peebles P. J., Ratra B., 2003, *Reviews of Modern Physics*, **75**, 559  
Perlmutter S., et al., 1999, *ApJ*, **517**, 565  
Planck Collaboration et al., 2014, *A&A*, **571**, A16  
Planck Collaboration et al., 2016a, *A&A*, **594**, A13  
Planck Collaboration et al., 2016b, *A&A*, **596**, A107  
Planck Collaboration et al., 2018, preprint, ([arXiv:1807.06209](https://arxiv.org/abs/1807.06209))  
Plionis M., Terlevich R., Basilakos S., Bresolin F., Terlevich E.,  
Melnick J., Chavez R., 2011, *MNRAS*, **416**, 2981  
Pryke C., Halverson N. W., Leitch E. M., Kovac J., Carlstrom  
J. E., Holzzapfel W. L., Dragovan M., 2002, *ApJ*, **568**, 46  
Reddy N. A., et al., 2015, *ApJ*, **806**, 259  
Riess A. G., et al., 1998, *AJ*, **116**, 1009  
Riess A. G., et al., 2011, *ApJ*, **730**, 119  
Riess A. G., et al., 2016, *ApJ*, **826**, 56  
Riess A. G., et al., 2018, *ApJ*, **855**, 136  
Salim S., Boquien M., Lee J. C., 2018, *ApJ*, **859**, 11  
Scolnic D. M., et al., 2018, *ApJ*, **859**, 101  
Scoville N., et al., 2007, *ApJS*, **172**, 1  
Shafer D. L., Huterer D., 2014, *Phys. Rev. D*, **89**, 063510  
Siegel E. R., Guzmán R., Gallego J. P., Orduña López M.,  
Rodríguez Hidalgo P., 2005, *MNRAS*, **356**, 1117  
Spergel D. N., et al., 2007, *ApJS*, **170**, 377  
Sullivan M., et al., 2011, *ApJ*, **737**, 102  
Suzuki N., et al., 2012, *ApJ*, **746**, 85  
Terlevich R., Terlevich E., Melnick J., Chávez R., Plionis M.,  
Bresolin F., Basilakos S., 2015, *MNRAS*, **451**, 3001  
Tresse L., Maddox S., Loveday J., Singleton C., 1999, *MNRAS*,  
**310**, 262  
Tu H., et al., 2009, *A&A*, **501**, 475  
Wang Y., Dai M., 2016, *Phys. Rev. D*, **94**, 083521  
Wang Y., Mukherjee P., 2006, *ApJ*, **650**, 1  
van der Wel A., et al., 2011, *ApJ*, **742**, 111

## APPENDIX A: INTERLOPERS IN THE 2D SPECTRA

Some of the 2D spectra show emission lines belonging to serendipitous objects, for example the one labeled Lensed target2. In our spectrum we observe the  $\text{HeI}\lambda 5876\text{\AA}$  emission line confirming the reported redshift of  $z=1.847$  given in (Brammer et al. 2012).

Another interesting object appears in the 2D spectrum of ZCOSMOS-411737; here we detected  $\text{H}\alpha$  and  $[\text{NII}]\lambda\lambda 6548,6584\text{\AA}$  lines at  $z=1.52$ .

In the 2D spectrum of COSMOS-19049, we detected emission lines corresponding to 4 objects at different redshifts. The first one presents  $[\text{O III}]\lambda\lambda 5007,4959\text{\AA}$  and  $\text{H}\beta$  at  $z=2.089$ . The second one shows only  $[\text{O III}]\lambda\lambda 5007,4959\text{\AA}$  at  $z=2.463$ . The third one present only one emission line which we propose that it is  $\text{H}\alpha$  at  $z=1.405$  although we do not rule out the possibility of it being  $[\text{O III}]\lambda 5007\text{\AA}$  at  $z=2.153$ . In this case  $[\text{O III}]\lambda 4959\text{\AA}$  would fall on a sky emission line, and  $\text{H}\beta$  would not have been detected if it was very faint. For the target object (COSMOS-19049 at  $z=1.369$ ) we detect  $\text{H}\alpha$ ,  $[\text{N II}]\lambda\lambda 6548,6584\text{\AA}$  and  $[\text{S II}]\lambda\lambda 6717,6731\text{\AA}$ .

In the 2D spectra of 3D-HST104245, UDS-109082, UDS23 and UDS-4501 we clearly see the continuum of other sources.

A faint emission line at  $\lambda_{obs}=16573.898\text{\AA}$  is seen in the 2D spectrum of UDS-14655. This line could be  $\text{H}\alpha$  at  $z=1.525$ ; however this identification is uncertain because it looks different to other  $\text{H}\alpha$  emitting objects at such redshift.

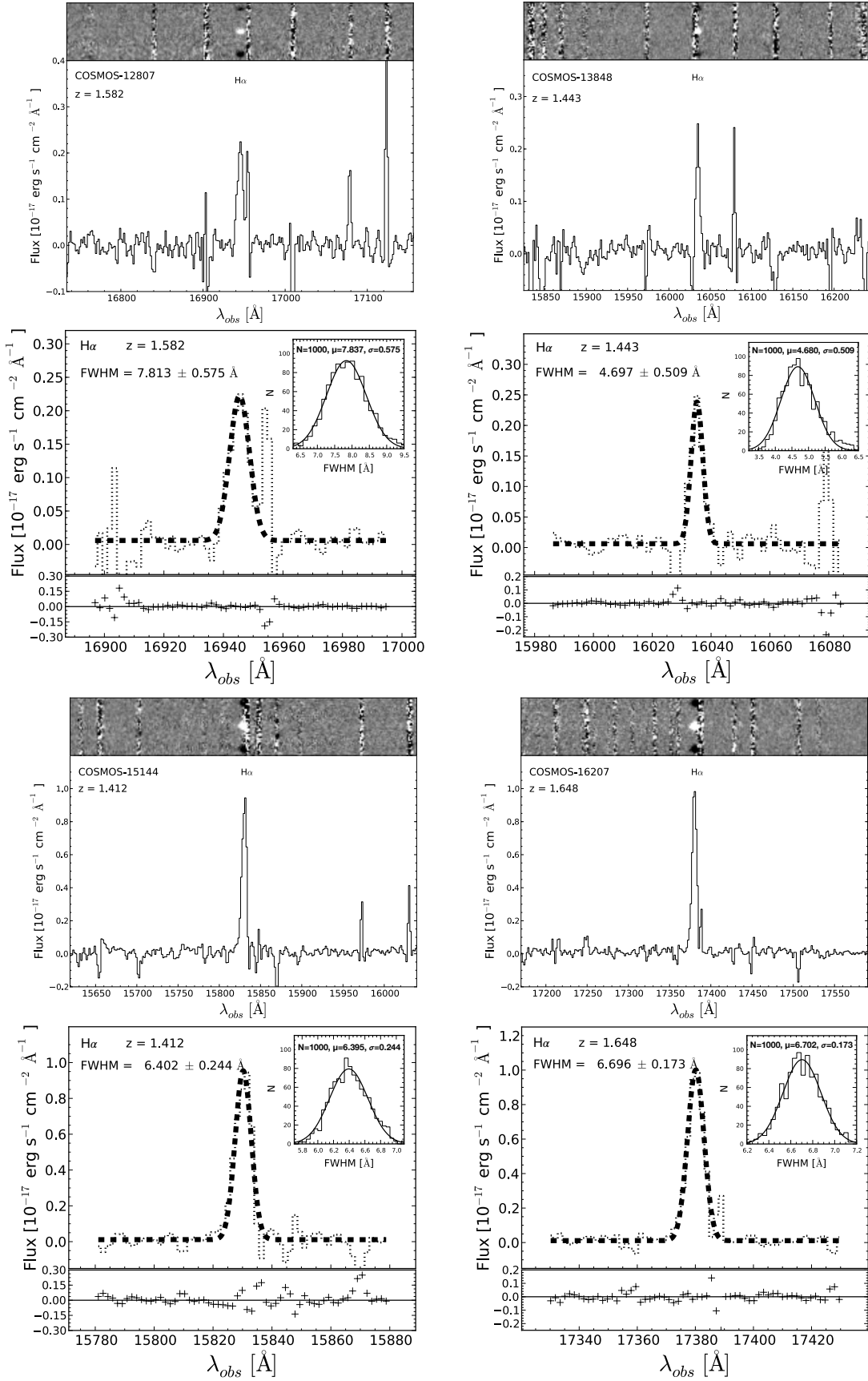
In the 2D spectrum of UDS-113972 we see an intense continuum and wide emission lines  $\text{H}\alpha$ ,  $[\text{N II}]\lambda\lambda 6548,6584\text{\AA}$  and  $[\text{S II}]\lambda\lambda 6717,6731\text{\AA}$  corresponding to an object at  $z=1.368$ .

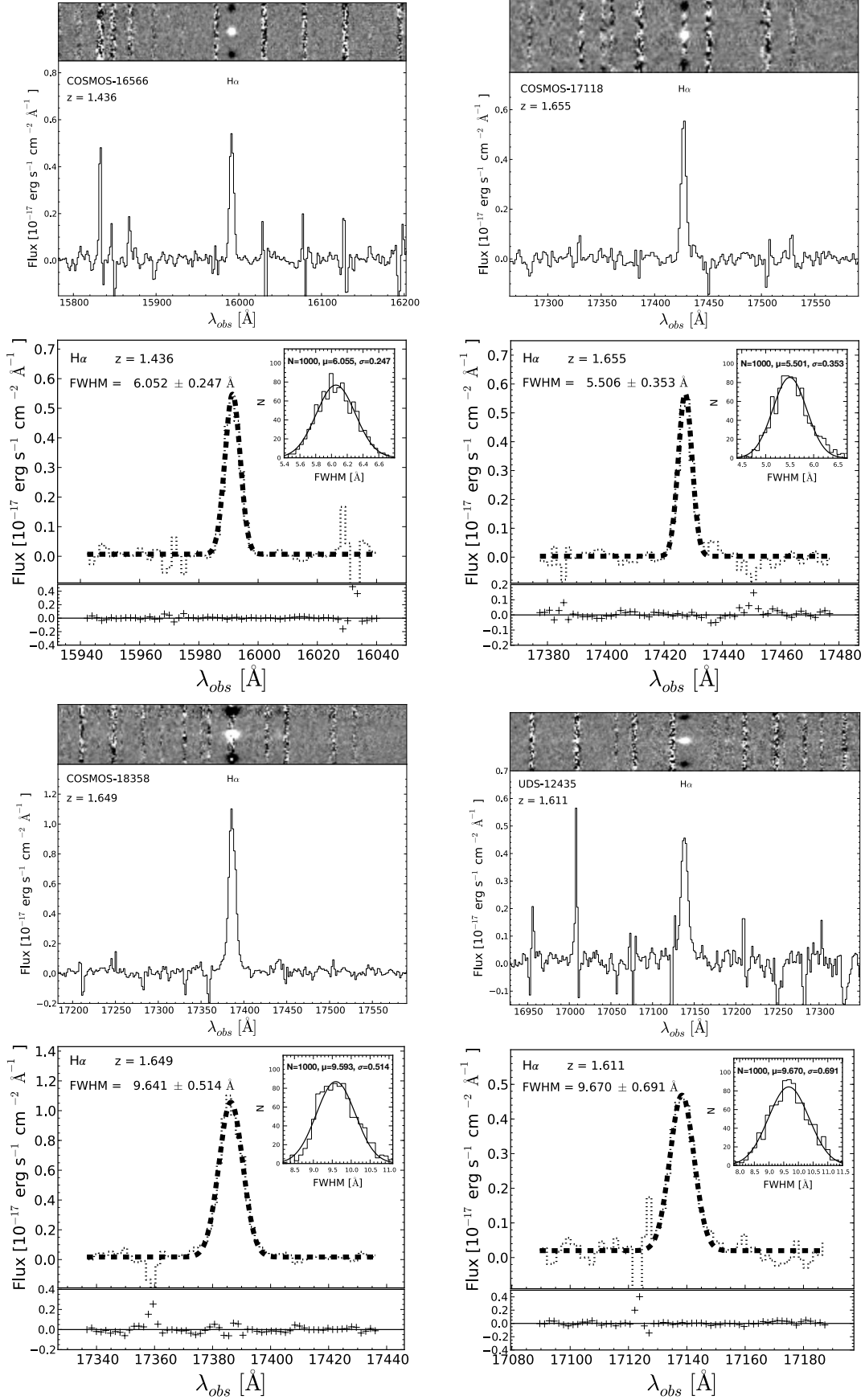
## APPENDIX B: MOSFIRE DATA

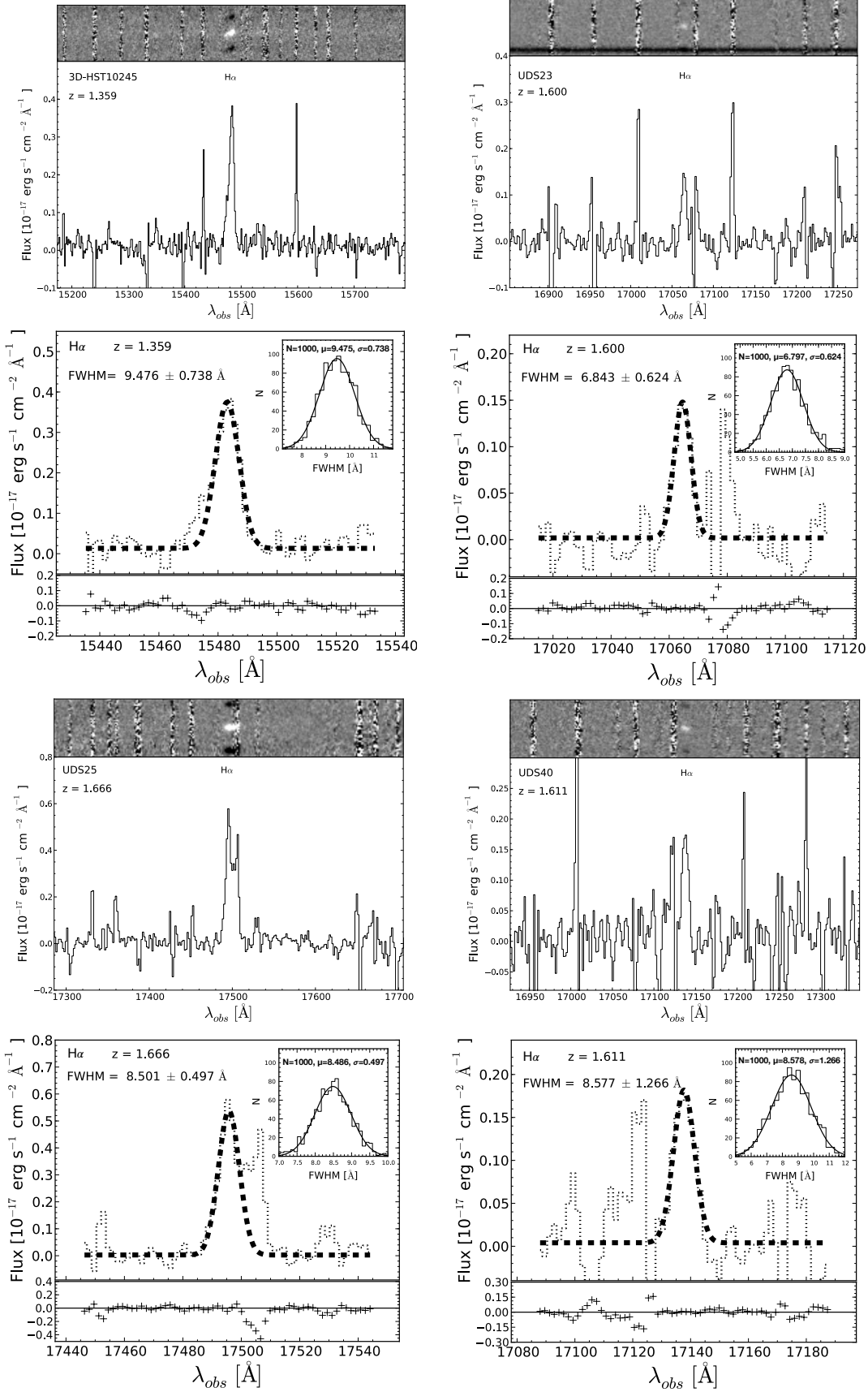
In this appendix we show for each HIIG the fits to the emission lines. We fitted  $\text{H}\alpha$  for the objects at  $z \sim 1.5$  and  $[\text{O III}]\lambda\lambda 4959,5007\text{\AA}$  and  $\text{H}\beta$  for the objects at  $z \sim 2.3$ .

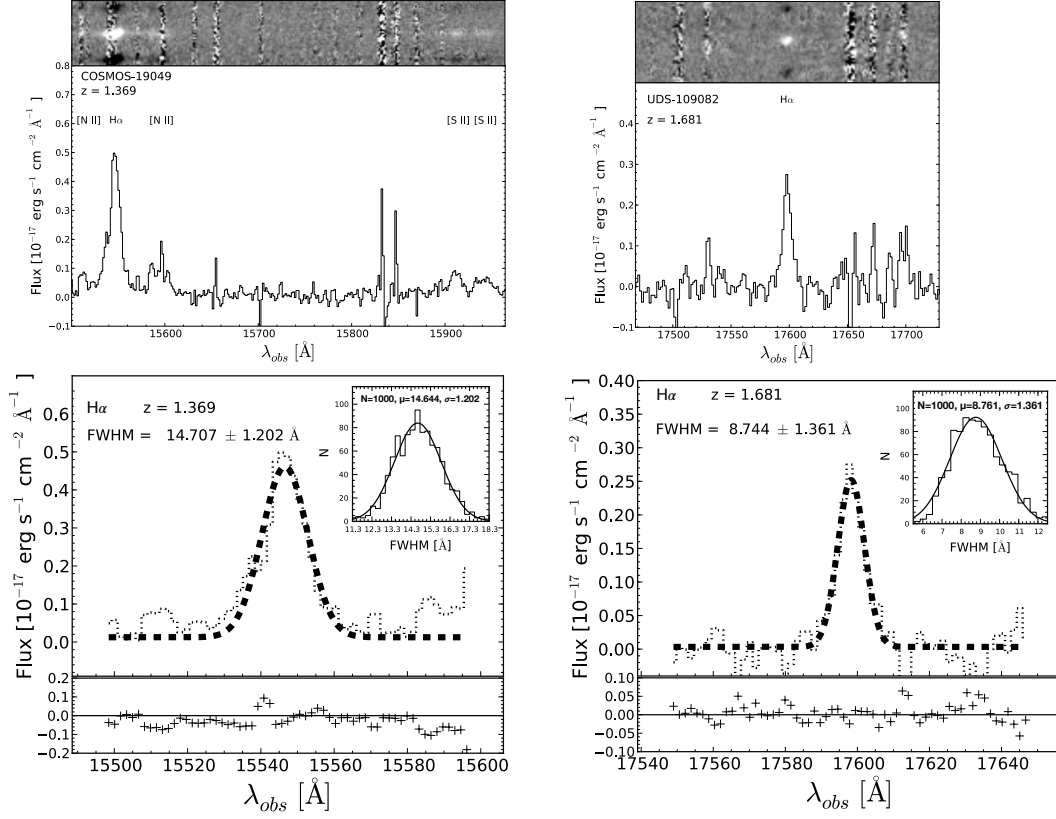
In the first and third rows (for objects at  $z \sim 1.5$ ) or in the first row (for objects at  $z \sim 2.3$ ), we present the 1D and 2D spectra.

In the second and fourth rows (for objects at  $z \sim 1.5$ ) or in the second, third and fourth columns (for objects at  $z \sim 2.3$ ), we show the fits to the  $\text{H}\alpha$  or  $[\text{O III}]\lambda\lambda 4959,5007\text{\AA}$  and  $\text{H}\beta$  emission lines, respectively. The residuals from the fits are shown in the lower panel. In the inset at the upper right corner we present the FWHM distribution from the Montecarlo simulations performed to estimate their errors.

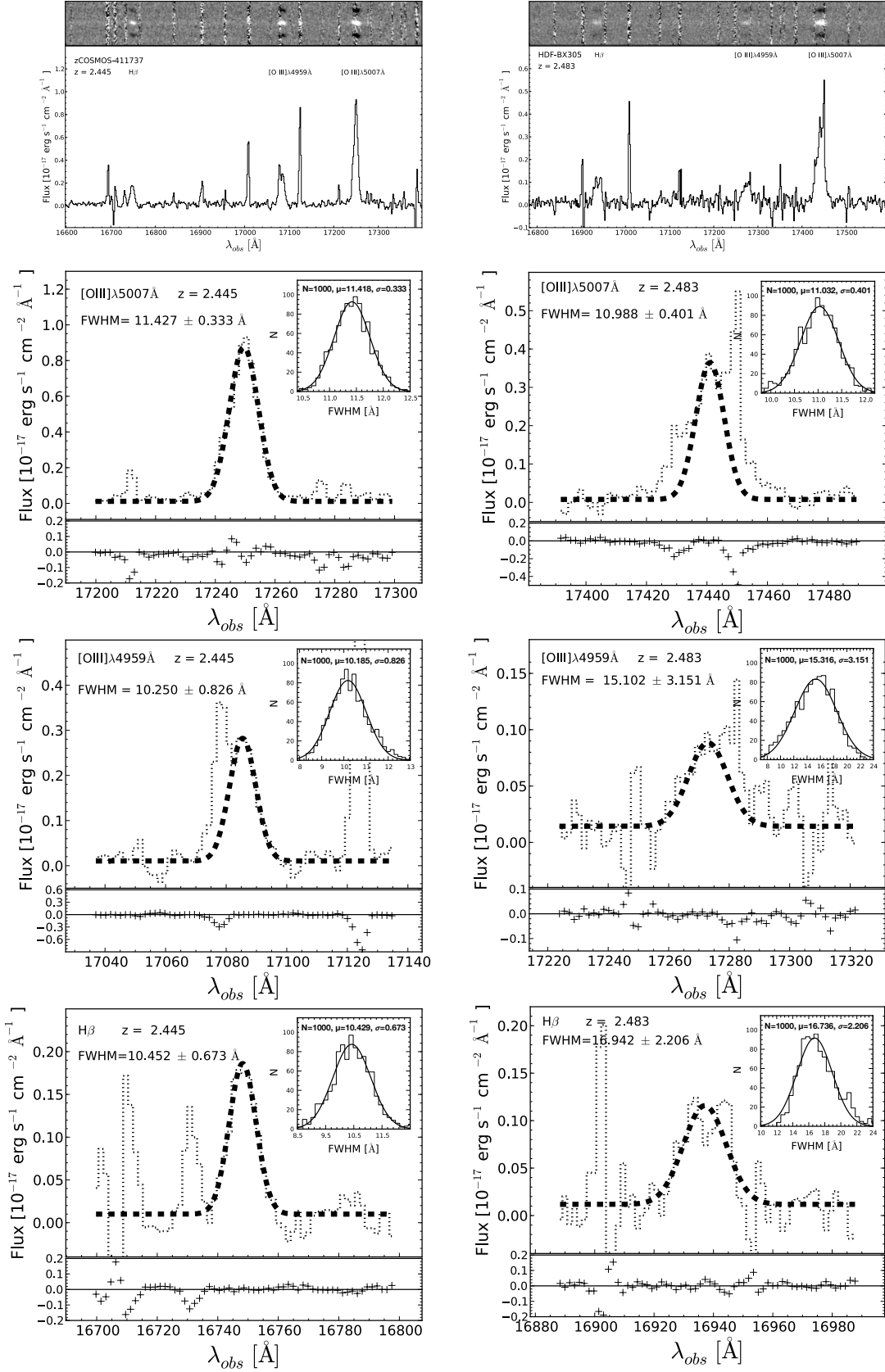


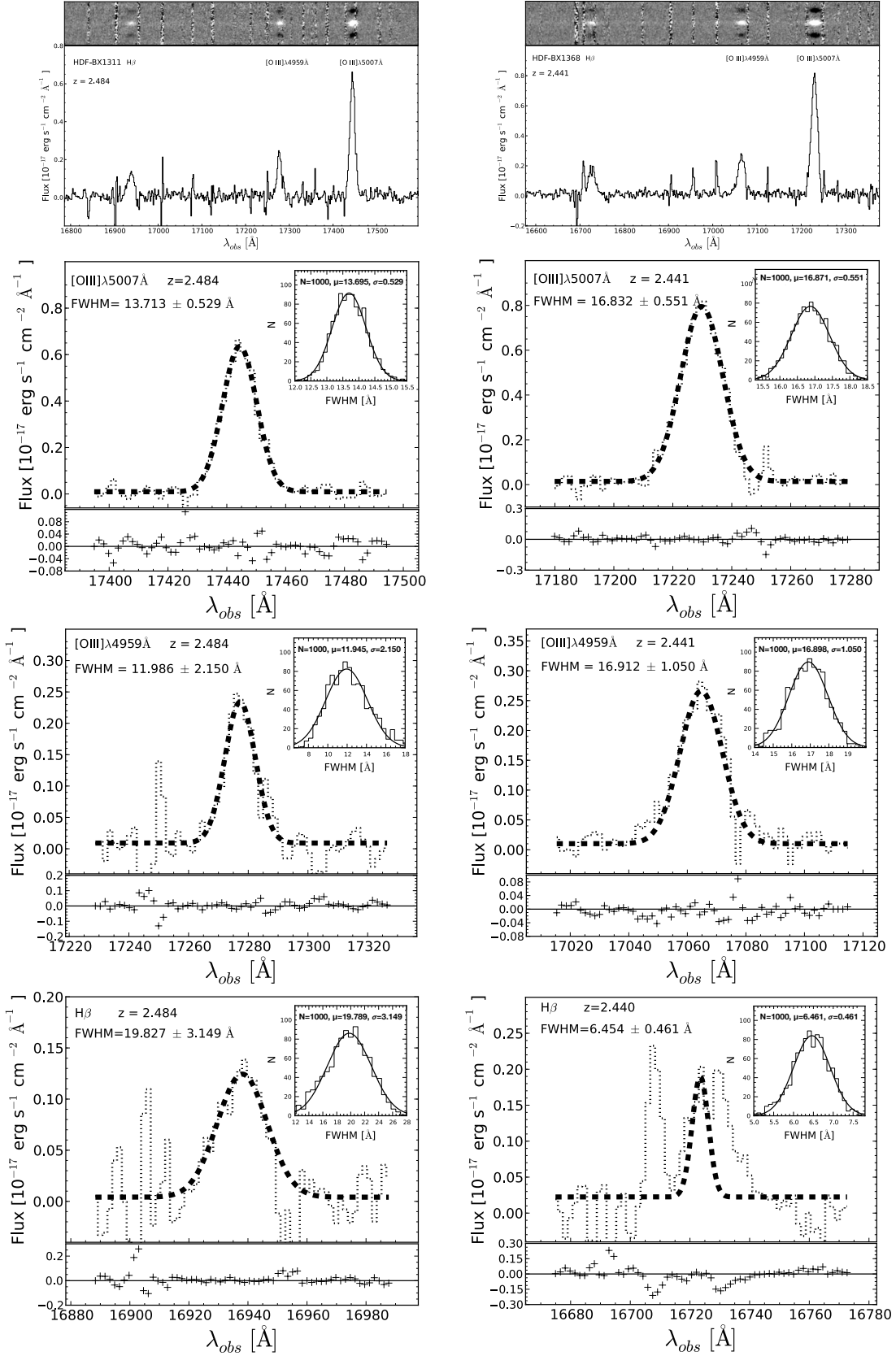


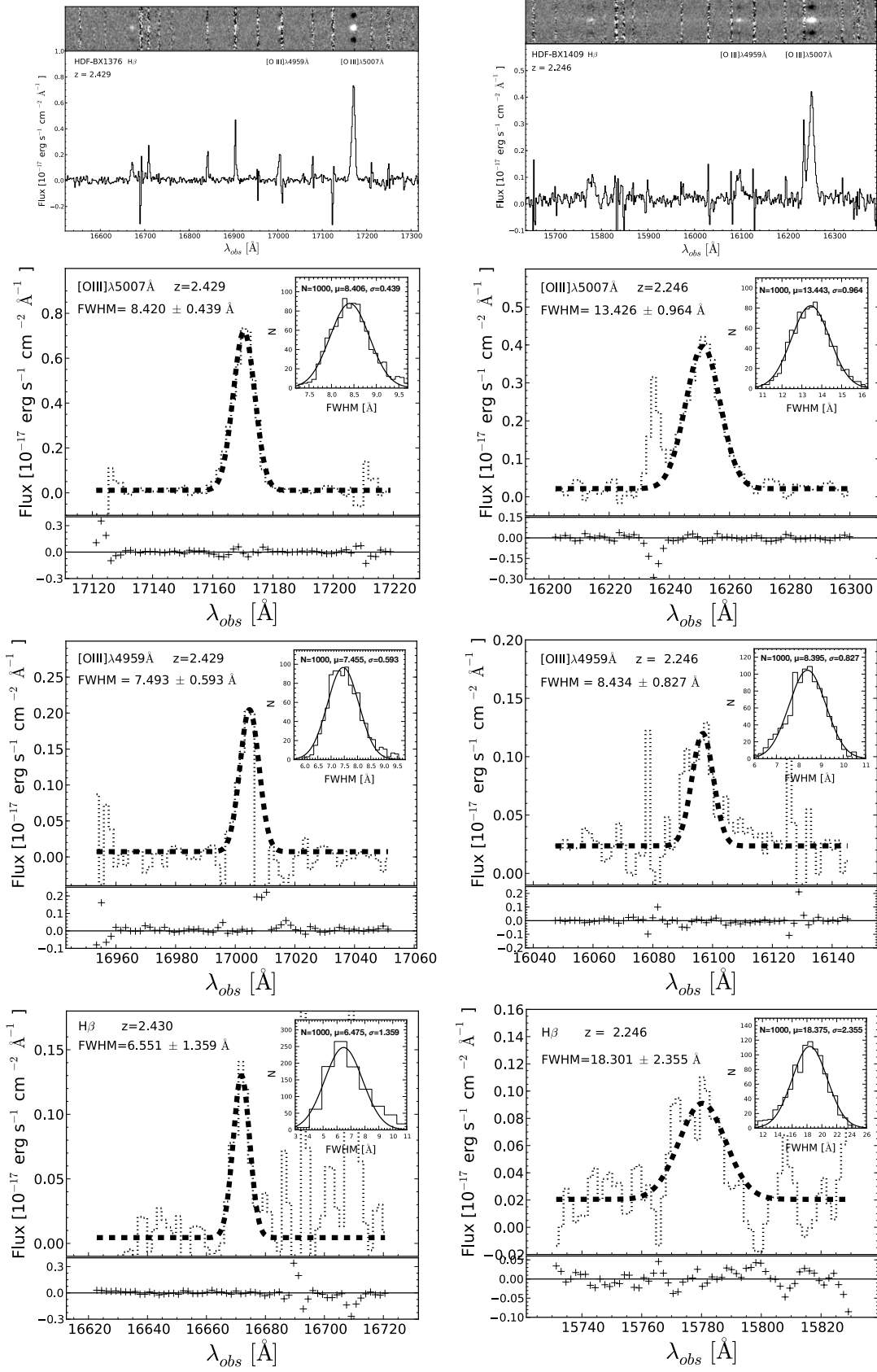


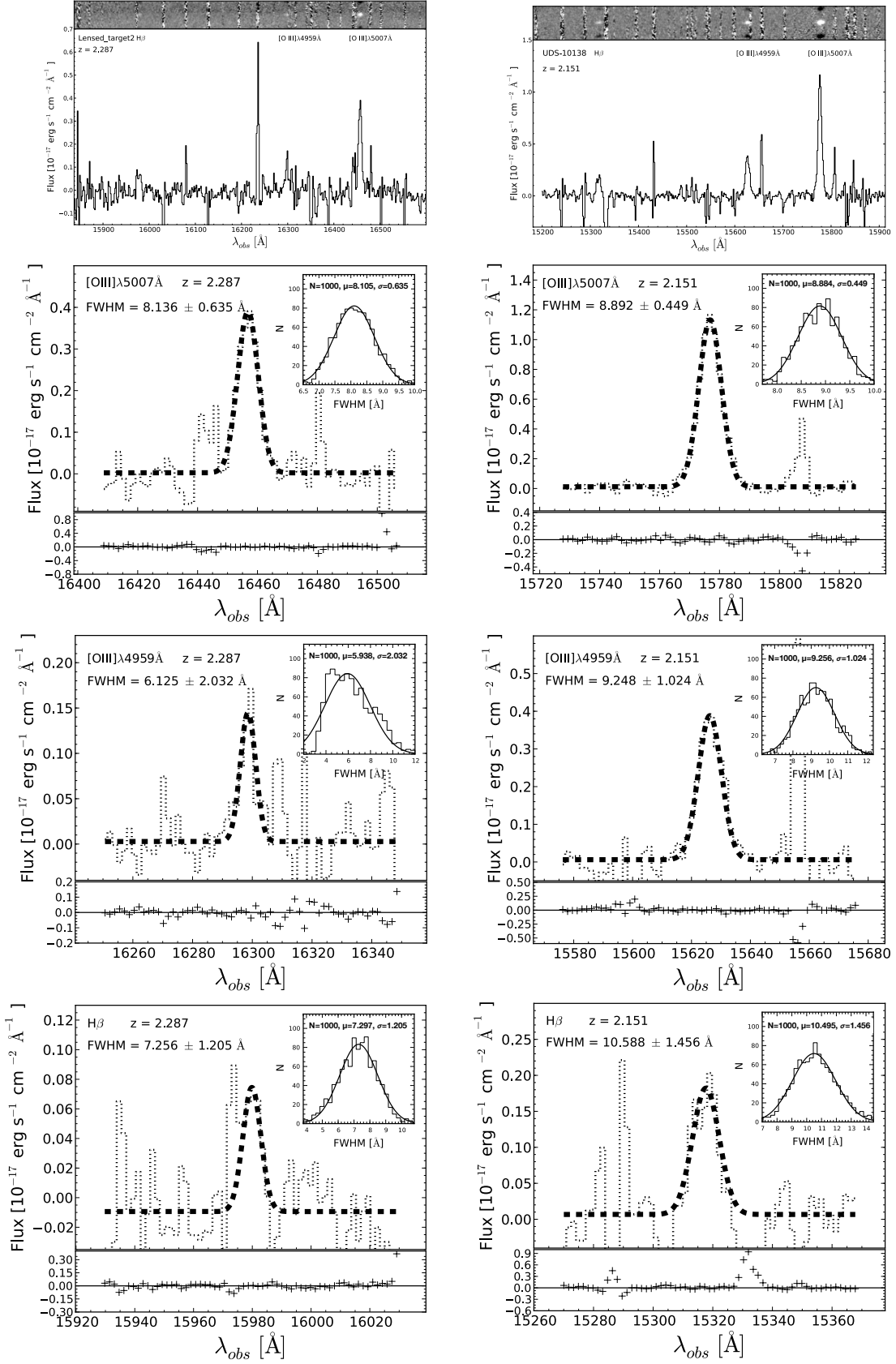


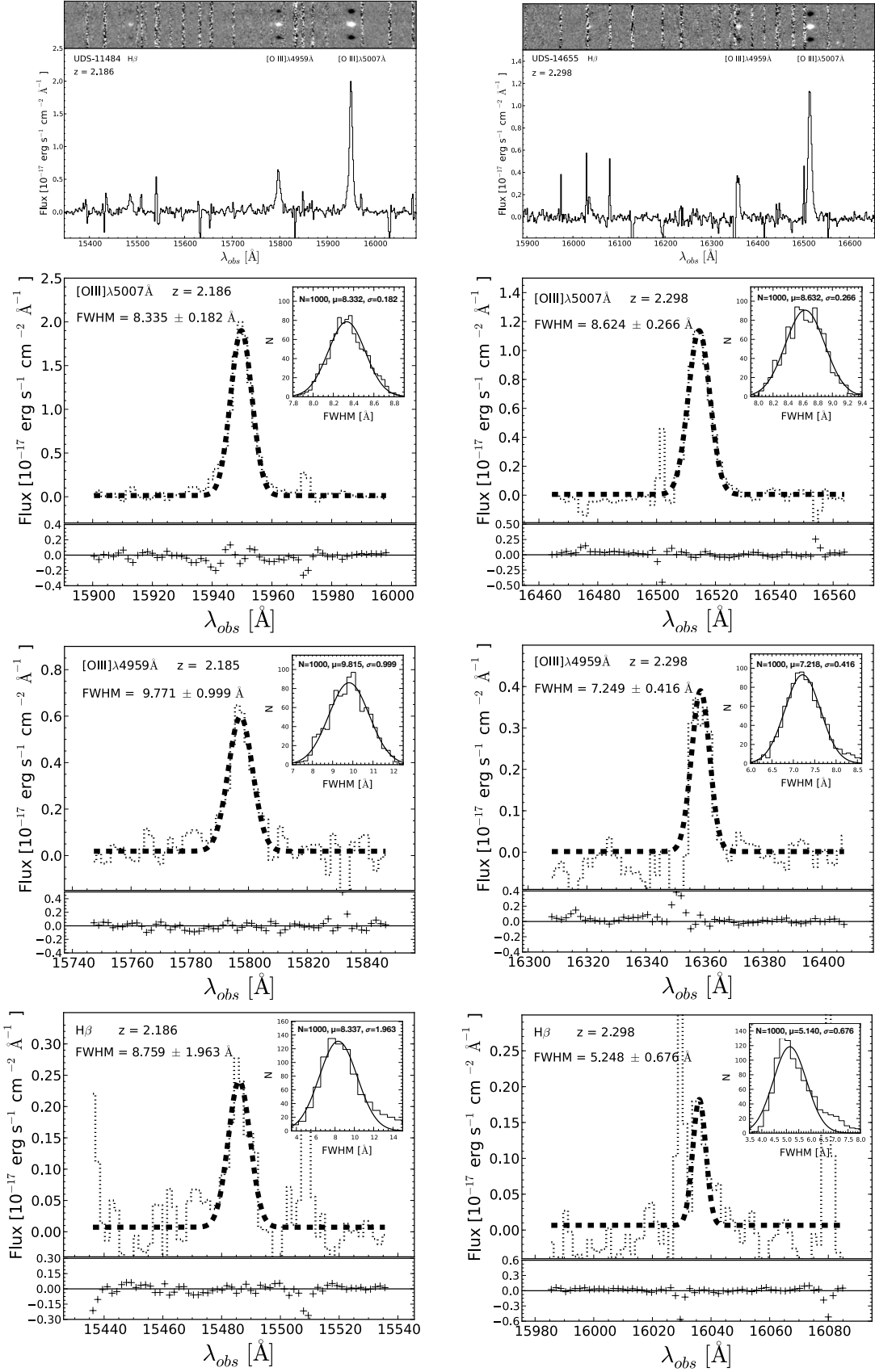
**Figure B1.** First and third rows show the H $\alpha$  1D and 2D spectra. Second and fourth rows show the fits to H $\alpha$ , the distribution of FWHM obtained from the Monte Carlo simulations in the inset at the upper right corner and the residuals in the box underneath.

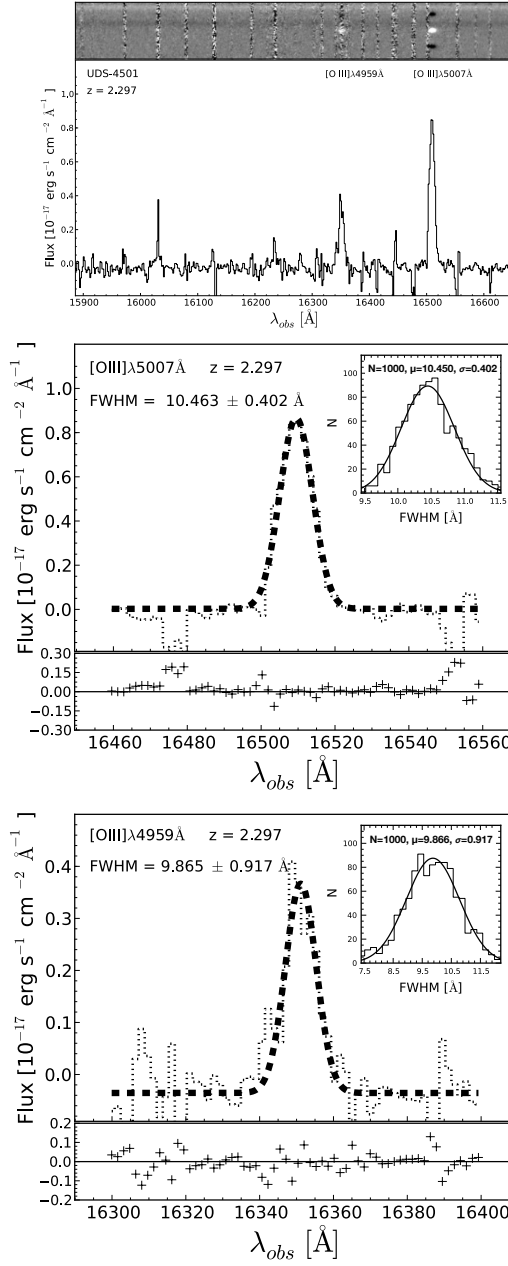












**Figure B2.** First row shows the 1D and 2D spectra of [O III] $\lambda\lambda 4959, 5007 \text{ \AA}$  and H $\beta$ . Second, third and fourth rows show the fits to the [O III] $\lambda\lambda 4959, 5007 \text{ \AA}$  and H $\beta$  lines, if detected, the distribution of FWHM obtained from the Monte Carlo simulations in the inset at the upper right corner and the residuals in the box underneath.